

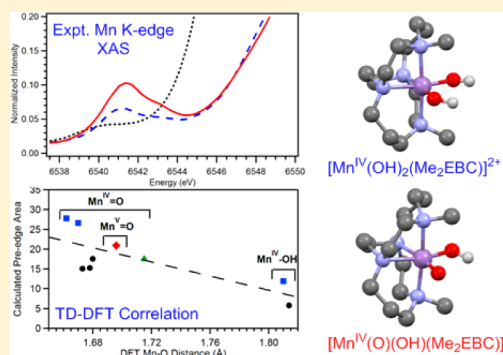
Mn K-Edge X-ray Absorption Studies of Oxo- and Hydroxo-manganese(IV) Complexes: Experimental and Theoretical Insights into Pre-Edge Properties

Domenick F. Leto and Timothy A. Jackson*

Department of Chemistry and Center for Environmentally Beneficial Catalysis, University of Kansas, Lawrence, Kansas 66045, United States

Supporting Information

ABSTRACT: Mn K-edge X-ray absorption spectroscopy (XAS) was used to gain insights into the geometric and electronic structures of $[\text{Mn}^{\text{II}}(\text{Cl})_2(\text{Me}_2\text{EBC})]$, $[\text{Mn}^{\text{IV}}(\text{OH})_2(\text{Me}_2\text{EBC})]^{2+}$, and $[\text{Mn}^{\text{IV}}(\text{O})(\text{OH})(\text{Me}_2\text{EBC})]^+$, which are all supported by the tetradentate, macrocyclic Me_2EBC ligand ($\text{Me}_2\text{EBC} = 4,11$ -dimethyl-1,4,8,11-tetraazabicyclo[6.6.2]hexadecane). Analysis of extended X-ray absorption fine structure (EXAFS) data for $[\text{Mn}^{\text{IV}}(\text{O})(\text{OH})(\text{Me}_2\text{EBC})]^+$ revealed Mn–O scatterers at 1.71 and 1.84 Å and Mn–N scatterers at 2.11 Å, providing the first unambiguous support for the formulation of this species as an oxohydroxomanganese(IV) adduct. EXAFS-determined structural parameters for $[\text{Mn}^{\text{II}}(\text{Cl})_2(\text{Me}_2\text{EBC})]$ and $[\text{Mn}^{\text{IV}}(\text{OH})_2(\text{Me}_2\text{EBC})]^{2+}$ are consistent with previously reported crystal structures. The Mn pre-edge energies and intensities of these complexes were examined within the context of data for other oxo- and hydroxomanganese(IV) adducts, and time-dependent density functional theory (TD-DFT) computations were used to predict pre-edge properties for all compounds considered. This combined experimental and computational analysis revealed a correlation between the Mn–O(H) distances and pre-edge peak areas of $\text{Mn}^{\text{IV}}=\text{O}$ and $\text{Mn}^{\text{IV}}-\text{OH}$ complexes, but this trend was strongly modulated by the Mn^{IV} coordination geometry. Mn 3d-4p mixing, which primarily accounts for the pre-edge intensities, is not solely a function of the Mn–O(H) bond length; the coordination geometry also has a large effect on the distribution of pre-edge intensity. For tetragonal $\text{Mn}^{\text{IV}}=\text{O}$ centers, more than 90% of the pre-edge intensity comes from excitations to the $\text{Mn}=\text{O} \sigma^*$ MO. Trigonal bipyramidal oxomanganese(IV) centers likewise feature excitations to the $\text{Mn}=\text{O} \sigma^*$ molecular orbital (MO) but also show intense transitions to $3d_{x^2-y^2}$ and $3d_{xy}$ MOs because of enhanced 3d-4p_{x,y} mixing. This gives rise to a broader pre-edge feature for trigonal $\text{Mn}^{\text{IV}}=\text{O}$ adducts. These results underscore the importance of reporting experimental pre-edge areas rather than peak heights. Finally, the TD-DFT method was applied to understand the pre-edge properties of a recently reported $S = 1$ $\text{Mn}^{\text{V}}=\text{O}$ adduct; these findings are discussed within the context of previous examinations of oxomanganese(V) complexes.



INTRODUCTION

Mn K-edge X-ray absorption spectroscopy (XAS) has featured prominently in the study of Mn enzymes and synthetic Mn compounds.^{1,2} For example, the oxygen-evolving complex (OEC) in photosystem II, which contains a $\text{Mn}_4\text{O}_5\text{Ca}$ cluster that converts H_2O to protons and O_2 , has been studied extensively by Mn XAS.^{3–7} These studies have provided important insights into structural changes in the OEC during the oxidation cycle and have highlighted the propensity for this cluster to undergo photodegradation upon X-ray irradiation.^{5–8} Mn XAS has also been widely utilized in the characterization of the bacterial enzyme Mn catalase (MnCAT), which employs a dimanganese active site to disproportionate H_2O_2 .^{1,9} Notably, XAS studies confirmed that the dimanganese(III,III) and dimanganese(II,II) forms of MnCAT are the active forms of the enzyme.⁹ With regard to synthetic systems, Mn K-edge XAS has played a critical role in the characterization of high-valent oxo- and hydroxo-manganese species^{10–16} that model intermediates commonly proposed in biological and synthetic

oxidation reactions.^{13,15,17–22} Although several $\text{Mn}^{\text{V}}-\text{oxo}$ adducts have been structurally characterized by X-ray diffraction,^{23–26} Mn K-edge XAS has been commonly employed to determine metal–ligand bond lengths for high-valent oxo- and hydroxo-manganese adducts that have thus far eluded structural characterization by X-ray diffraction.^{10–22,27} A major advantage of the XAS technique is that crystalline samples are not required.

K-edge XAS spectra are divided into two regions: the extended X-ray absorption fine structure (EXAFS) region, which occurs beyond the K-edge; and the X-ray absorption near edge structure (XANES) region, which is within ~ 10 eV of the K-edge. Analysis of EXAFS and XANES data provide complementary information about the metal center. Accurate (~ 0.02 Å) metal–ligand and, in the case of multinuclear species, metal–metal distances can be extracted from the

Received: March 24, 2014

Published: June 5, 2014

EXAFS region,²⁸ while the XANES region is reflective of the oxidation state and coordination environment of the metal. The energy of the absorption K-edge (metal 1s-to-4p transition) is sensitive to the effective nuclear charge of the absorbing metal atom due to 1s core-hole shielding effects.⁵ Pre-edge features, which commonly occur ~10 eV before the edge, arise from electric-quadrupole-allowed metal 1s-to-3d transitions that have a low intrinsic XAS intensity. However, these electric-dipole (parity) forbidden metal 1s-to-3d transitions can gain intensity through metal 3d-4p mixing induced by low symmetry distortions and/or be mediated by metal–ligand covalency.^{29–33} Thus, the pre-edge energy and intensity, and edge energy, are useful probes of metal oxidation state, site geometry, and metal–ligand covalency. However, the fact that the XANES properties are not isolated signatures of a single property of the metal center, but instead are impacted by a conglomerate of effects, complicates the analysis of XANES data.^{31,34} Consequently, the pre-edge region is often used to infer changes in the metal oxidation state and/or site geometry by comparisons with well-characterized model compounds. XAS studies of Mn^V–oxo and –nitrido model complexes have revealed intense pre-edge features that are attributed to short axial Mn–oxo and Mn–nitrido distances.^{35–37} However, the lack of an intense pre-edge feature does not confirm the absence of a Mn^V–oxo species. For example, the presence of a sixth ligand *trans* to the oxo in [Mn^V(O)(TDCPP)] (TDCPP = meso-tetrakis(2,6-dichlorophenyl)porphinato dianion) significantly diminished the Mn pre-edge intensity.³⁸ Thus, care must be taken when inferring specific structural motifs on the basis of pre-edge data alone.

A detailed and quantitative analysis of the pre-edge region involving a complement of experiment and theory can provide significant insight into the electronic structure of the metal.^{29–31,33} Detailed experimental and computational analysis of the pre-edge regions of Fe K-edge spectra has proven to be a valuable tool for studying the electronic and geometric structure of Fe^{IV}–oxo complexes.^{39–41} In addition, such an analysis provides insight into the physical basis for pre-edge properties, rather than treating such data at a phenomenological level. Application of this combined experimental and theoretical approach to the analysis of the pre-edge regions of high-valent Mn K-edge spectra is limited to formally Mn^V–oxo and Mn^V–nitrido complexes,^{37,42} as well as Mn^{IV} dithiolene complexes.⁴³ Such studies have been enabled by recently described time-dependent density functional theory (TD-DFT) methods that have been successfully used for the accurate prediction of pre-edge properties for a variety of monomeric Fe compounds^{29,30} and monomeric and dimeric Mn compounds.^{34,44} Notably, Roemelt and co-workers established and validated a TD-DFT method for a set of 16 monomeric Mn(II) and Mn(III) compounds, successfully reproducing the shape, intensity, and energy of the experimental pre-edge spectra.³⁴

In this current work, Mn K-edge XAS and TD-DFT methods are used to explore the geometric and electronic structure of a pair of hydroxo- and oxomanganese(IV) complexes, [Mn^{IV}(OH)₂(Me₂EBC)]²⁺ (**2**) and [Mn^{IV}(O)(OH)(Me₂EBC)]⁺ (**3**), that are supported by the ethylene cross-bridged macrocyclic ligand Me₂EBC (Me₂EBC is 4,11-dimethyl-1,4,8,11-tetraazabicyclo[6.6.2]hexadecane) and differ only by a proton (Figure 1). [Mn^{II}(Cl₂)(Me₂EBC)] (**1**), from which **2** and **3** are derived, is included in the analysis for comparison. While the crystal structures of **1** and **2** have been reported,^{27,45} the EXAFS data presented here provide the first

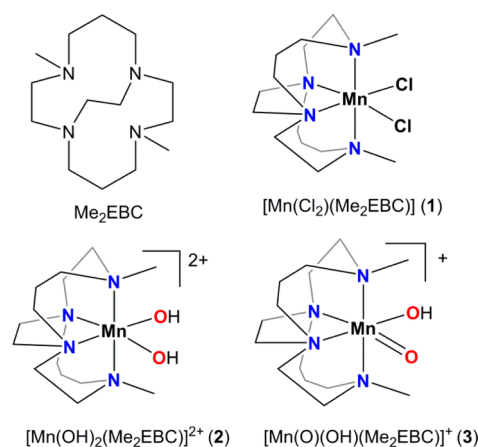


Figure 1. Structure of Me₂EBC ligand and complexes [Mn^{II}(Cl₂)(Me₂EBC)] (**1**), [Mn^{IV}(OH)₂(Me₂EBC)]²⁺ (**2**), and [Mn^{IV}(O)(OH)(Me₂EBC)]⁺ (**3**).

structural parameters for **3**, adding to the limited structural information available for monomeric Mn^{IV}–oxo complexes.^{10–16} To gain insight into the nature of the pre-edge transitions of these complexes, and to explore the Mn pre-edge properties of manganese(IV) complexes in general, we performed TD-DFT calculations for **2** and **3**, as well as for a set of oxo- and hydroxo-manganese(IV) complexes with diverse geometries and supporting ligands. Good agreement is observed between the experimental and calculated XANES spectra, indicating that the TD-DFT method is robust in predicting pre-edge spectra for high-valent Mn complexes. The effects of coordination geometry and ligand properties on pre-edge transitions of Mn^{IV}–oxo and Mn^{IV}–hydroxo species are discussed.

EXPERIMENTAL AND COMPUTATIONAL METHODS

Materials. [Mn^{IV}(OH)₂(Me₂EBC)](PF₆)₂ was generated by oxidizing [Mn^{II}(Cl₂)(Me₂EBC)] (**1**) with H₂O₂ (30% aqueous solution) in the presence of NH₄PF₆ in deionized H₂O, as described previously.⁴⁵ [Mn^{IV}(O)(OH)(Me₂EBC)]⁺ (**3**) was prepared by adjusting the pH of an aqueous solution of **2** to 8.8 with 0.3 M NaOH.^{18,45} **2** has a pK_a in water of 6.86(4), ensuring >98% formation of **3** at a pH of 8.8.^{18,27}

Mn K-Edge XAS Experiments. A 2% (w/w) dispersion of **1** in boron nitride was prepared by grinding 4 mg of **1** with 196 mg of boron nitride into a fine powder with a mortar and pestle. For the EXAFS sample of **2**, a 29 mM solution of **2** was prepared by dissolving 9.6 mg of the PF₆[−] salt of **2** in 0.5 mL of deionized H₂O at 25 °C. Approximately 200 μL of this solution was transferred to an XAS sample holder. The XANES sample of **2** was prepared from a 9.7 mM aqueous solution of **2**. For the EXAFS sample of **3**, an 8.4 mM solution of **3** was prepared by dissolving 26.8 mg of the PF₆[−] salt of **2** in 5 mL of deionized H₂O at 25 °C. The pH was adjusted to 8.8 by the addition of 0.3 M NaOH (0.140 mL). The formation of **3** from **2** was monitored by electronic absorption spectroscopy. Once the formation of **3** was completed, five samples were prepared by transferring approximately 200 μL of **3** into separate XAS sample holders. The XANES sample of **3** (pH = 8.8) was prepared by adjusting the pH of a 9.7 mM aqueous solution of **2** with 0.3 M NaOH to a final pH of 8.8. All samples were immediately flash-frozen in liquid N₂ and stored under liquid nitrogen prior to XAS data collection.

XAS Data Collection. EXAFS and XANES spectra were recorded on beamline X3B at the National Synchrotron Light Source (NSLS), Brookhaven National Lab (storage ring conditions, 2.8 GeV, 100–300 mA). Mn K-edge X-ray absorption spectra over the energy range 6.4–

7.4 keV (Si(111) monochromator) were recorded on frozen solutions, or, in the case of **1**, a powder sample, maintained at 20 K with a helium Displex closed-cycle cryostat. For EXAFS data, XAS spectra were obtained as fluorescence excitation spectra using either a solid-state 13-element (**1**) or a 31-element (**2** and **3**) germanium detector (Canberra). Contamination of higher harmonics radiation was minimized by using a harmonic rejection mirror. The background fluorescence signal was reduced by use of a 6 μm chromium filter for **1** and **2** and a 3 μm filter for **3**. A manganese foil spectrum was recorded concomitantly for internal energy calibration, and the first inflection point of the K-edge energy was assigned to 6539.0 eV. Spectra were measured with 5 eV steps below the edge (6359–6529 eV), 0.3 eV steps in the edge region (6529–6564 eV), and steps equivalent to 0.05 \AA^{-1} increments above the edge. The X-ray flux at 6.6–7.1 keV was $2(1) \times 10^{10}$ photons \times s $^{-1}$ \times mm $^{-2}$. Under these conditions, it was observed that complex **3** was photoreduced after each 50 min scan, as the edge energy shifted \sim 0.9 eV to lower energy in the second scan and shifted \sim 0.3 eV to lower energy in subsequent scans on the same spot. Thus, the effects of photoreduction on the EXAFS data set were minimized by reducing the X-ray flux and collecting only one scan per sample spot on three different samples for complex **3**. The EXAFS spectra of complexes **1** (2% w/w in boron nitride), **2** (29 mM in H₂O), and **3** (8.4 mM in H₂O, pH 8.8) represent the average of 8, 12, and 11 scans, respectively. To investigate the photoreduction of **3**, five sequential scans, under conditions of high X-ray flux, were collected on the same sample spot for two different samples.

Additional Mn K-edge XANES data, which provided higher resolution over a wider energy window, were obtained for 9.7 mM frozen aqueous solutions of **2** and **3** using a solid-state 31-element germanium detector (Canberra) with a 3 μm chromium filter. Spectra were measured with 5 eV steps below the edge (6359–6518 eV), 0.3 eV steps in the edge region (6518–6569 eV), steps equivalent to 0.05 \AA^{-1} increments above the edge (6569–6676 eV), and steps equivalent to 0.1 \AA^{-1} increments at higher energy. The XANES spectrum of **2** represents the average of four consecutive scans from one sample. The XANES spectrum of **3** represents the average of six scans from six sample spots collected under conditions of low X-ray flux.

EXAFS Data Analysis. EXAFS data reduction and averaging were performed using the program EXAFSPAK.⁴⁶ Pre-edge background intensity was removed by fitting a Gaussian function to the pre-edge background and subtracting this function from the whole spectrum. The spectrum was then fit with a three-segment spline with fourth-order polynomial components to remove low-frequency background. EXAFS refinement was carried out on $k^3\chi(k)$ data, using phase and amplitude functions obtained from *FEFF*, version 6,⁴⁷ and structural models of **1**, **2**, and **3** obtained from DFT geometry optimizations (*vide infra*). For each fit, the parameters r (average distance between Mn and scattering atom) and σ^2 (Debye–Waller factor) were optimized, while n , the number of atoms in the shell, was kept fixed. n was varied by integer steps systematically. The goodness-of-fit (GOF) was evaluated by the parameter F , where $F = \sum (\chi_{\text{calcd}} - \chi_{\text{expt}})^2 / N$, and N is the number of data points. The threshold energy, E_0 , in electronvolts ($k = 0$ point) was kept at a common, variable value for every shell of a given fit.

XANES Data Analysis. Mn K-edge pre-edge data were fit using EDG_FIT in EXAFSPAK.⁴⁶ Second derivative spectra were used to help determine the number and position of peaks. Pre-edge features were fit using pseudo-Voigt line shapes (sums of Lorentzian and Gaussian functions), and the energy position, full width at half-maximum (fwhm), and peak height were varied.³¹ A fixed 1:1 ratio of Lorentzian to Gaussian functions successfully reproduced the pre-edge features. The rising edge and background under the pre-edge features were also fit with pseudo-Voigt line shapes. Good fits reproduced the pre-edge features using a minimum number of peaks. The fits were performed over three energy ranges, and reported peak area (height \times fwhm) and peak energy are based on the average of all three fits.

Computations. All DFT calculations were carried out using the ORCA program package, versions 2.8 and 2.9.⁴⁸ Full geometry optimizations were performed using the Becke–Perdew (BP86) functional^{49,50} in conjunction with the TZVP (for Mn, N, O, and

Cl) and SVP (for C and H) basis sets^{51,52} and were treated at the spin-unrestricted level. Because these calculations employed a resolution of the identity approximation (RI),⁵³ the SV/J and TZV/J auxiliary basis sets were also used.^{51,52} All optimizations were performed without symmetry constraints. Numerical frequency calculations were performed on all optimized structures to ensure that the optimized structures represent true minima. A dense integration grid (ORCA Grid5) and tight convergence criteria were enforced for all geometry optimizations. Calculations were converged to the $S = 5/2$ state for **1** (high-spin Mn^{II}) and the $S = 3/2$ state for all Mn^{IV} complexes.

The crystal-structure coordinates of **1**⁵⁴ and **2**²⁷ were utilized as starting points for full geometry optimizations. Previously published DFT geometry-optimized coordinates were used as initial structures of **3**,¹⁸ [Mn^{IV}(O)(N4py)]²⁺,¹⁵ [Mn^{IV}(O)(Bn-TPEN)]²⁺,¹⁶ and the models were subjected to full geometry optimization. Models of [Mn^{IV}(O)(salen)] and [Mn^{IV}(OH)(salen)]⁺ were built by replacing the aqua ligand in the XRD structure of [Mn^{III}(OH₂)(salen)]⁺ with an oxo and hydroxo ligand, respectively.¹⁴ For [Mn^{IV}(O)(T_{piv}PP)],¹⁰ an initial model was constructed using the known structure of the ligand and DFT geometry-optimizations were performed. The initial model of [Mn^{IV}(O)(H₃buea)]⁻ was built by replacing Fe^{III} with Mn^{IV} in the DFT-optimized coordinates of [Fe^{III}(O)(H₃buea)]²⁻.⁵⁵ From the optimized coordinates of [Mn^{IV}(O)(H₃buea)]⁻, the model of [Mn^V(O)(H₃buea)] was optimized to the $S = 1$ spin state.

To reduce the computational cost of the TD-DFT computations for the salen- and porphyrin-containing complexes, the salen ligand in the optimized models of [Mn^{IV}(O)(salen)] and [Mn^{IV}(OH)(salen)]⁺ was truncated by replacing the mesityl groups with methyl groups. In addition, the porphyrinic ligand in the optimized model of [Mn^{IV}(O)(T_{piv}PP)] was truncated by replacing the pivalamidophenyl groups with methyl groups. After truncation, full DFT geometry-optimizations were performed.

XAS Calculations. The Mn K pre-edge spectra were calculated using the TD-DFT method within the Tamm–Dancoff approximation.^{56,57} The B3LYP functional^{58–60} and def2-SVP (for C and H) and def2-TZVP(-f) (for Mn, N, O, and Cl) basis sets were utilized for these calculations.⁶¹ Scalar relativistic effects were taken into account at the ZORA level,^{62,63} and a dense integration grid (ORCA Grid4) and tight convergence criteria were enforced. As established previously, the calculated spectra were shifted 32.6 eV to higher energy to correct for systematic errors in the level of theory (i.e., density functional, basis set, etc.).³⁴ The calculated spectra using def2-SVP (for C and H) and def2-TZVP(-f) (for Mn, N, O, and Cl) basis sets were \sim 0.2 eV lower in energy than the calculated spectra using the larger def2-TZVP(-f) basis set for all atoms (Figure S1 in Supporting Information), within the error of the energy correction of 32.6 ± 0.2 eV.³⁴ Computed Mn K pre-edge data were plotted by applying a Gaussian fit with a 1 eV broadening, which provides a good comparison with previous TD-DFT calculations of pre-edge properties.^{34,44,55} The calculated intensities include electric dipole, electric quadrupole, and magnetic dipole contributions, as described in the Supporting Information. The calculated area (A) was obtained from the calculated intensity (I) according to the correlation $A = 6.01I + 1.79$, as established for a set of monomeric Mn(II) and Mn(III) compounds.³⁴ MO plots were generated using the program gOpenMol.

To determine if truncation of the salen ligand had a significant effect on the calculated pre-edge spectrum of [Mn^{IV}(O)(salen)], TD-DFT calculations were performed using a DFT-optimized model of the full, untruncated [Mn^{IV}(O)(salen)] model. The calculated pre-edge intensity for the truncated model of [Mn^{IV}(O)(salen)] was within 5% of the calculated intensity for the complete complex of [Mn^{IV}(O)(salen)] (Figure S2, Supporting Information), indicating a marginal impact on the pre-edge intensity due to the truncation. Thus, unless noted otherwise, calculations for the salen- and porphyrin-containing complexes were performed using truncated versions of the ligand. When the TD-DFT calculations for [Mn^{IV}(O)(H₃buea)]⁻ were carried out in a continuum dielectric using the conductor like screening model COSMO,⁶⁴ with dimethylformamide as the solvent, the energy of the individual transitions decreased by >0.1 eV. The pre-

edge intensity decreased by $\sim 10\%$ relative to the gas-phase calculation (Figure S1, bottom).

RESULTS AND ANALYSIS

1. Experimental XAS Data. (A). EXAFS Data and Fitting Results for 1, 2, and 3. The Fourier transform (R' space) of the EXAFS spectrum of **1** exhibits a broad peak at $R' \approx 2.0$ Å that is best accounted for by two shells of scatterers 2.47 (two Cl scatterers) and 2.29 Å (four N scatterers), as shown in Figure 2A and Table 1. The distances of the Cl and N scatterers

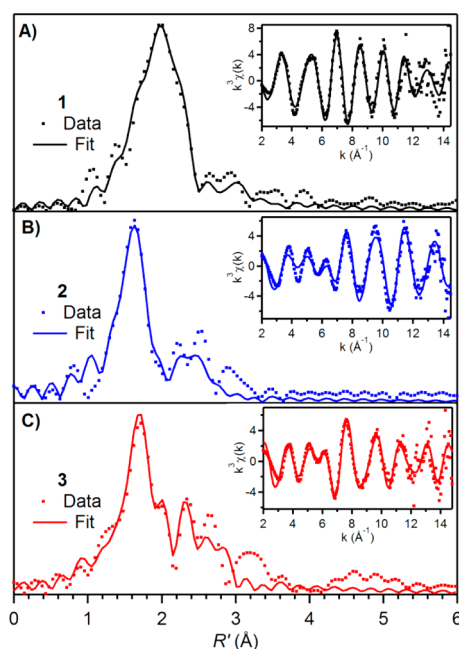


Figure 2. Fourier transforms of Mn K-edge EXAFS data [$k^3\chi(k)$] and raw EXAFS spectra (insets), experimental data (···) and fits (—) for (A) $[\text{Mn}^{\text{II}}(\text{Cl})_2(\text{Me}_2\text{EBC})]$ (**1**), (B) $[\text{Mn}^{\text{IV}}(\text{OH})_2(\text{Me}_2\text{EBC})]^{2+}$ (**2**), and (C) $[\text{Mn}^{\text{IV}}(\text{O})(\text{OH})(\text{Me}_2\text{EBC})]^+$ (**3**). Details regarding EXAFS fits are in Table 1.

are in good agreement with the average Mn–Cl and Mn–N distances of 2.455 and 2.334 Å observed in the X-ray diffraction structure of **1** (Table 2).⁵⁴ Fits modeling the two smaller peaks at $R' \approx 2.6$ and 2.9 Å using two Mn···C shells at 3.03 and 3.21 Å (4 and 6 C atoms, respectively) improve the overall goodness-of-fit (Table 1 and Table S1, Supporting Information). In the X-ray diffraction structure of **1**, two C atoms are located at a Mn···C distance of ~ 3.00 Å, 10 C atoms at Mn···C distances ranging from 3.10 to 3.26 Å (average Mn···C distance 3.18 Å), and 2 C atoms are located at a Mn···C distance of ~ 3.65 Å.⁵⁴ Thus, all structural parameters obtained from EXAFS fits of **1** are in excellent agreement with the corresponding XRD structure.

The Fourier-transformed EXAFS spectrum of **2** exhibits a sharp peak centered at $R' \approx 1.6$ Å with less prominent peaks at $R' \approx 2.2$, 2.5, and 2.9 Å (Figure 2B). The prominent FT peak at ~ 1.6 Å arises from the first-coordination sphere and is best fit with two shells of N/O scatterers at distances of 1.80 Å, corresponding to the pair of hydroxo ligands, and 2.08 Å, corresponding to the four nitrogen atoms of the tetradentate Me_2EBC ligand (Table 1). These Mn–ligand distances compare quite favorably to the corresponding distances observed in the X-ray structure of **2**, which had Mn–OH and

average Mn–N distances of 1.811 and 2.10 Å, respectively (Table 2).²⁷ The shorter Mn–N distances of **2** compared to **1** are expected given the increase in the Mn oxidation state (from 2+ to 4+) and the concomitant reduction in ionic radius. The less-prominent FT peaks in the EXAFS spectrum of **2** at $R' \approx 2.2$ and 2.5 Å are best fit with a single shell of six C atoms at 2.94 Å. In the X-ray diffraction structure of **2**, 12 C atoms of the ligand are located at Mn···C distances ranging between 2.86–3.04 Å (average Mn···C distance 2.97 Å) and two C atoms of the ligand are located at a Mn···C distance of 3.47 Å.

With the limited stability of **3** in basic media, structural analysis by X-ray diffraction has not been possible.⁴⁵ Thus, the EXAFS data described here provide the first Mn–ligand bond lengths for **3**. The Fourier-transformed EXAFS spectrum of **3** exhibits a sharp peak centered at $R' \approx 1.7$ Å with a shoulder at ~ 2.0 Å and weaker features at 2.3, 2.6, and 3.2 Å (Figure 2C). The first coordination sphere of **3** is best fit with three shells of N/O atoms at distances of 1.71 (one O scatterer), 1.84 (one O scatterer), and 2.11 Å (four N scatterers). The shells at 1.71 and 1.84 Å are best fit with one oxygen atom each, corresponding to the oxo and hydroxo ligands, respectively. Fits with only a single shell of two O atoms resulted in a Mn–O distance of 1.77 Å with an unreasonably high Debye–Waller factor (8.11×10^{-3} Å²; Fit 1 in Table 1). The EXAFS data for **3** also require two Mn···C shells at 2.88 and 3.02 Å (4 and 6 C atoms, respectively).

Metric parameters from the EXAFS data of **3** are in good agreement with a structure derived from DFT computations (Table 2).¹⁸ The DFT-optimized structure of **3** features a Mn=O distance of 1.682 Å, slightly shorter than the EXAFS-determined distance of 1.71 Å. The short Mn=O distance in **3**, as compared to the Mn–OH distances in **2**, is indicative of the expected Mn=O double-bond character and is consistent with Mn^{IV}=O bond lengths observed for other Mn(IV) centers with terminal oxo ligands (1.673–1.706 Å by DFT computations; 1.69 Å from EXAFS analysis).^{10,15,16,20} The computed 1.838 Å Mn–OH bond length in **3** is in excellent agreement with the EXAFS-determined distance (1.84 Å). The DFT-computed model of **3** shows a longer Mn–N distance *trans* to the oxo ligand (2.261 Å), an expected outcome of the strong donating ability of the oxo ligand. However, the EXAFS data for **3** are best fit with only a single shell of N scatterers, and thus, this computational prediction is not directly verifiable.

(B). X-ray Photoreduction of 3. Although **2** showed no evidence of photoreduction in 12 sequential scans on one spot of one sample, **3** was readily photoreduced under identical experimental conditions (at 20 K and with the same X-ray flux). Thus, the data described above were collected under conditions of reduced X-ray flux and by irradiating separate spots on the sample. Under conditions of high flux, photoreduction of **3** was evident by a 0.9 eV red-shift in the edge energy on the second scan (Figure 3). No shift was observed in the position of the pre-edge peak, but the intensity of this feature decreased in subsequent scans (Figure 3). In sequential scans, the edge energy red-shifted in approximately 0.3 eV increments, and the pre-edge peak intensity continued to decrease.⁶⁵ Photoreduction of high-valent Mn complexes has been observed previously.^{1,6,7,15,28,66} Elegant XAS studies of the Mn₄Ca-containing OEC have shown that system to be very sensitive to X-ray photoreduction.²⁸ Indeed, upon high-flux X-ray irradiation, the XANES properties of the OEC convert from those characteristic of the oxo-bridged cluster to signals most consistent with aqueous Mn(II); i.e., the cluster is almost

Table 1. EXAFS Fitting Results for $[\text{Mn}^{\text{II}}(\text{Cl}_2)(\text{Me}_2\text{EBC})]$ (**1**), $[\text{Mn}^{\text{IV}}(\text{OH})_2(\text{Me}_2\text{EBC})]^{2+}$ (**2**), and $[\text{Mn}^{\text{IV}}(\text{O})(\text{OH})(\text{Me}_2\text{EBC})]^{+}$ (**3**)^a

1										
fit ^b	Mn–Cl			Mn–N			Mn···C			F-factor
	<i>n</i>	<i>r</i> (Å)	$\sigma^2 \times 10^3$ (Å ²)	<i>n</i>	<i>r</i> (Å)	$\sigma^2 \times 10^3$ (Å ²)	<i>n</i>	<i>r</i> (Å)	$\sigma^2 \times 10^3$ (Å ²)	
1				6	2.36	1.73				0.497
2	2	2.47	1.52	4	2.28	4.42				0.407
4	2	2.47	1.70	4	2.30	4.48	4	3.22	3.20	0.383
5	2	2.47	1.76	4	2.30	4.53	6	3.18	9.77	0.383
9	2	2.47	1.42	4	2.29	4.19	4	3.03	3.05	0.359
							6	3.21	2.78	
2										
fit ^b	Mn–O			Mn–N			Mn···C			F-factor
	<i>n</i>	<i>r</i> (Å)	$\sigma^2 \times 10^3$ (Å ²)	<i>n</i>	<i>r</i> (Å)	$\sigma^2 \times 10^3$ (Å ²)	<i>n</i>	<i>r</i> (Å)	$\sigma^2 \times 10^3$ (Å ²)	
1				6	1.99	1.94				0.701
2	2	1.79	1.04	4	2.08	3.30				0.502
7	2	1.80	0.95	4	2.08	3.64	4	2.94	3.64	0.441
8	2	1.80	0.92	4	2.08	3.67	6	2.94	6.89	0.436
3										
fit ^b	Mn–O			Mn–N			Mn···C			F-factor
	<i>n</i>	<i>r</i> (Å)	$\sigma^2 \times 10^3$ (Å ²)	<i>n</i>	<i>r</i> (Å)	$\sigma^2 \times 10^3$ (Å ²)	<i>n</i>	<i>r</i> (Å)	$\sigma^2 \times 10^3$ (Å ²)	
1	2	1.77	8.11	4	2.12	2.44				0.583
2	1	1.71	1.49	4	2.11	2.56				0.572
	1	1.84	1.61							
3	1	1.72	1.44	4	2.11	2.86	4	3.02	2.64	0.481
	1	1.84	1.21							
4	1	1.72	1.45	4	2.11	2.83	5	3.02	4.03	0.487
	1	1.84	1.26							
10	1	1.71	1.53	4	2.11	2.68	4	2.88	4.04	0.468
	1	1.84	1.44				6	3.02	2.54	

^aFourier transform ranges as follows: 1: 2–14.5 Å⁻¹ (resolution 0.126 Å); 2: 2–14.8 Å⁻¹ (resolution 0.123 Å); 3: 2–14.8 Å⁻¹ (resolution 0.123 Å).

^bThe fit number is in reference to all fits considered, as presented in Supporting Information (Table S1).

completely destroyed upon prolonged X-ray irradiation. It is, to us, unexpected that the monocationic complex **3** should be more susceptible to X-ray photoreduction than the dicationic complex **2**. In addition, the dramatic change in photostability between **2** and **3**, which differ only by a H⁺, was not anticipated. The observed experimental behavior underscores the need to use caution when performing X-ray studies of higher oxidation state manganese centers, as it is challenging to predict when photoreduction will readily occur.

(C). *Experimental XANES Data.* The Mn K-edge XANES of **1**, **2**, and **3** are shown in Figure 4 and summarized in Table 3. The XANES spectrum of the manganese(II) complex **1** displays a small pre-edge feature with low intensity at 6540.4 eV and the intense rising edge feature at 6547.1 eV. The pre-edge and edge energies are consistent with other six-coordinate Mn(II) complexes.³⁴ The energies of the edge and pre-edge features of **2** are respectively blue-shifted by almost 5 eV (6552.0 eV) and 0.6 eV (6541.0 eV) relative to **1**, as expected for the higher Mn oxidation state in **2**. In addition to the blue-shift in pre-edge energy, a notable increase in the pre-edge height is observed, and fits of the pre-edge region reveal a shoulder at 6543.2 eV (Figure S3). The edge energy of **3** (6551.8 eV) is nearly equivalent to that of **2**, although the pre-edge peak of **3** (6541.2 eV) is double the intensity of that of **2** and has a resolved shoulder at 6543.3 eV (Table 3). As the intensity of the pre-edge features of both **2** and **3** are too great to arise from electric-quadrupole transitions,^{44,67} their intensity

likely derives through Mn 4p-3d mixing allowed by low symmetry distortions. Because electric-dipole transitions are substantially more intense than electric-quadrupole transitions,^{44,67} only a small amount of 3d-4p mixing is required to cause a sizable increase in pre-edge peak intensity.³¹ Because the Mn oxidation state and coordination number remain unchanged between **3** and **2**, the dramatic increase in pre-edge intensity for the former complex is attributed to the short Mn^{IV}=O distance of 1.71 Å (Table 2), which introduces a large deviation from centrosymmetry.

(D). *Comparison of Experimental Pre-edge and Edge Energies.* To date, only a handful of monomeric oxo- and hydroxo-manganese(IV) complexes have been studied by XAS, and all these complexes feature either a pseudo-octahedral or square pyramidal coordination geometry.^{10,14–16} The structures of these complexes are shown in Scheme 1. The oxomanganese(IV) complexes fall into three classes: (i) six-coordinate oxomanganese(IV) complexes supported by neutral aminopyridyl NS ligands ($[\text{Mn}^{\text{IV}}(\text{O})(\text{N}4\text{py})]^{2+}$ and $[\text{Mn}^{\text{IV}}(\text{O})(\text{Bn-TPEN})]^{2+}$, where N4py = *N,N*-bis(2-pyridylmethyl)-*N*-bis(2-pyridyl)methylamine and Bn-TPEN = *N*-benzyl-*N,N,N'*-tris(2-pyridylmethyl)-1,2-diaminoethane);^{15,16} (ii) six-coordinate complexes with an N₄O⁻ coordination sphere (**2**); and (iii) five-coordinate, square pyramidal complexes supported by dianionic ligands ($[\text{Mn}^{\text{IV}}(\text{O})(\text{salen})]$ and $[\text{Mn}^{\text{IV}}(\text{O})(\text{T}_{\text{piv}}\text{PP})]$, where salen = bis(3,5-dimesitylsalicylidene)-1,2-dimesitylethylenediamine and T_{piv}PP = the *meso*-tetra(α,α,α-pivalamido-

Table 2. Comparison of Mn-Ligand Bond Lengths from X-ray Diffraction (XRD), EXAFS fits and DFT Computations for $[\text{Mn}^{\text{II}}(\text{Cl}_2)(\text{Me}_2\text{EBC})]$ (1), $[\text{Mn}^{\text{IV}}(\text{OH})_2(\text{Me}_2\text{EBC})]^{2+}$ (2), and $[\text{Mn}^{\text{IV}}(\text{O})(\text{OH})(\text{Me}_2\text{EBC})]^+$ (3)

1^a	XRD (Å)	EXAFS (Å)	DFT (Å)
Mn–Cl(1)	2.456(2)	2.47	2.509
Mn–Cl(2)	2.455(2)	2.47	2.509
Mn–N(3)	2.347(4)	2.29	2.436
Mn–N(4)	2.333(4)	2.29	2.436
Mn–N(5)	2.325(4)	2.29	2.367
Mn–N(6)	2.332(4)	2.29	2.367
2^b			
Mn–OH(1)	1.811(2)	1.80	1.814
Mn–OH(2)	1.811(2)	1.80	1.814
Mn–N(3)	2.110(3)	2.08	2.205
Mn–N(4)	2.110(3)	2.08	2.205
Mn–N(5)	2.090(2)	2.08	2.139
Mn–N(6)	2.090(2)	2.08	2.139
3^c			
Mn–O(1)		1.71	1.682
Mn–OH(2)		1.84	1.838
Mn–N(3)		2.11	2.156
Mn–N(4)		2.11	2.150
Mn–N(5)		2.11	2.184
Mn–N(6)		2.11	2.261

^aXRD data from ref 54. ^bXRD data from ref 27; DFT structure from ref 18. ^cDFT structure from ref 18.

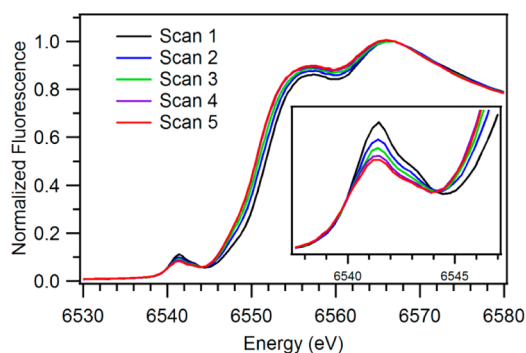


Figure 3. Mn K-edge XANES spectra of 3 as it is photoreduced. Each trace represents the average of two scans collected from different sample spots.

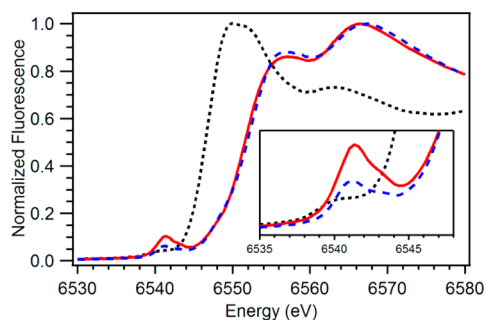


Figure 4. Mn K-edge XANES of $[\text{Mn}^{\text{II}}(\text{Cl}_2)(\text{Me}_2\text{EBC})]$ (1; black, dotted line), $[\text{Mn}^{\text{IV}}(\text{OH})_2(\text{Me}_2\text{EBC})]^{2+}$ (2; blue, dashed line), and $[\text{Mn}^{\text{IV}}(\text{O})(\text{OH})(\text{Me}_2\text{EBC})]^+$ (3; red, solid line) obtained at 20 K.

phenyl-porphyrinato) dianion).^{10,14} Although none of these complexes have been characterized crystallographically, their

structures are inferred on the basis of spectroscopic data and, in some cases, DFT-derived models.

For this series of oxomanganese(IV) complexes, the observed pre-edge and edge energies span a range of 3 eV (6538.9–6541.9 eV) and approximately 2 eV (6549.9–6552.0 eV), respectively (see Table 3). The pre-edge energy decreases with the overall charge on the oxomanganese(IV) complex, with the highest energies observed for the dicationic complexes $[\text{Mn}^{\text{IV}}(\text{O})(\text{N4py})]^{2+}$ and $[\text{Mn}^{\text{IV}}(\text{O})(\text{Bn-TPEN})]^{2+}$ (6541.9 and 6541.6 eV, respectively).^{15,16} The monocationic complex 3 shows only a marginally lower pre-edge peak energy (6541.2 eV), and the neutral $[\text{Mn}^{\text{IV}}(\text{O})(\text{salen})]$ complex has the lowest pre-edge energy by far (6538.9 eV). It should be noted, however, that the $[\text{Mn}^{\text{IV}}(\text{O})(\text{salen})]$ XAS spectrum was calibrated to Cu foil (8978.9 eV), whereas the other oxomanganese(IV) complexes were calibrated either to the K-edge energy of the first inflection point of a manganese foil spectrum (6539.0 eV)^{10,14,15} or to the pre-edge peak maximum of a KMnO_4 powder spectrum (6543.3 eV).¹⁶ Thus, the low pre-edge energy of $[\text{Mn}^{\text{IV}}(\text{O})(\text{salen})]$ is potentially an artifact of calibration since the XAS data were calibrated to a standard at much higher energy than the other Mn(IV) samples. Although different beamlines were used to collect the XAS data for these eight Mn(IV) complexes (Table 3), comparing data from multiple beamlines is common practice.²⁹ In a separate study, Cu foil XAS spectra, measured at 11 different beamlines, showed only subtle changes in the edge shape and pre-edge intensity.⁶⁸ Nonetheless, we cannot unambiguously rule out that different data collection, refinement, and analysis procedures could complicate the comparison of pre-edge properties of the Mn-salen complexes.

(E). Comparison of Experimental Pre-edge Intensities. Because the pre-edge peak height of 3 is nearly double that of 2 (0.103 and 0.066 for the height of the pre-edge peak maxima; see Table 3), it is unexpected that the pre-edge peak height of $[\text{Mn}^{\text{IV}}(\text{O})(\text{salen})]$ is nearly equivalent to that of $[\text{Mn}^{\text{IV}}(\text{OH})(\text{salen})]^+$ (0.046 and 0.044, respectively). Self-absorption effects are not expected to have a significant impact on the pre-edge peak heights for these samples, as the XAS data were collected on dilute frozen solutions. The similarities in peak height for these salen complexes are even more unusual given that EXAFS data for the $[\text{Mn}^{\text{IV}}(\text{O})(\text{salen})]$ complex were fit to give a Mn=O distance of 1.58 Å (the corresponding Mn–OH distance in $[\text{Mn}^{\text{IV}}(\text{OH})(\text{salen})]^+$ is 1.83 Å).¹⁴ The 1.58 Å distance is quite short for a $\text{Mn}^{\text{IV}}=\text{O}$ species.^{10,15,16} While a very pronounced pre-edge feature would be expected for such a short $\text{Mn}^{\text{IV}}=\text{O}$ distance, mitigating factors such as the influence of the metal coordination environment or Mn-salen covalency could potentially modulate the pre-edge intensity. These complexities underscore the need for a combined experimental and theoretical analysis of $\text{Mn}^{\text{IV}}=\text{O}$ complexes to investigate the physical basis for pre-edge properties.

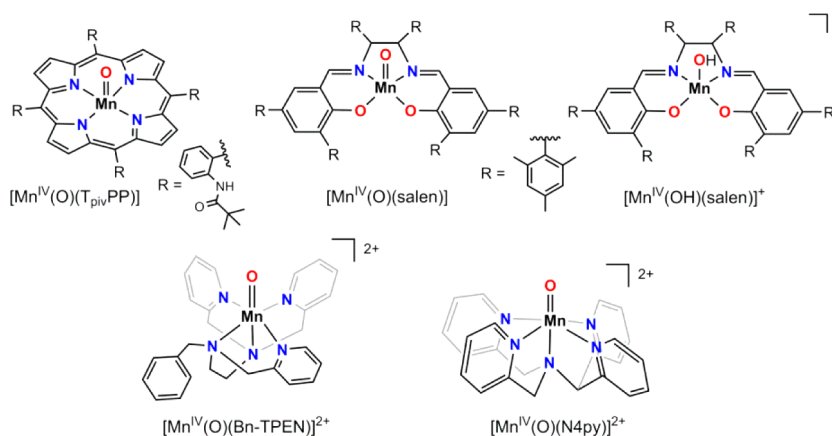
2. TD-DFT-Computed Mn Pre-edge Spectra. (A). Calculated Pre-edge Properties for 1, 2, and 3. General Considerations. To explore the performance of TD-DFT calculations for the pre-edge properties of Mn^{IV} centers, and to gain insight into the origin of pre-edge transitions for these complexes, we first compare the calculated Mn pre-edge features of 2 and 3 with those observed experimentally (calculations for complex 1 were also performed for comparison). These complexes serve as excellent points for validation, as they are structurally characterized (1 and 2 by XRD and EXAFS, and 3 by EXAFS alone), and the Mn-ligand

Table 3. Mn Edge and Pre-edge Properties of $[\text{Mn}^{\text{II}}(\text{Cl}_2)(\text{Me}_2\text{EBC})]$ (1), $[\text{Mn}^{\text{IV}}(\text{OH})_2(\text{Me}_2\text{EBC})]^{2+}$ (2), $[\text{Mn}^{\text{IV}}(\text{O})(\text{OH})(\text{Me}_2\text{EBC})]^+$ (3) and other $\text{Mn}^{\text{IV}}=\text{O}$ and $\text{Mn}^{\text{IV}}-\text{OH}$ complexes (see Scheme 1)

	edge energy (eV)	pre-edge energy (eV)	pre-edge peak height ^a	area ^b	ref
1	6547.1	6540.4	0.041	3.9	c
2	6552.0	6541.0	0.066	5.0	c
3	6551.8	6543.2	0.052	2.0	c
		6541.2	0.103	10.5	
		6543.3	0.072	3.7	
$[\text{Mn}^{\text{IV}}(\text{O})(\text{N4py})]^{2+}$ ^f	6550.8	6541.9	0.077	12.7	15
$[\text{Mn}^{\text{IV}}(\text{O})(\text{Bn-TPEN})]^{2+}$ ^g	NR ^d	6541.6	NR ^d	NR ^d	16
$[\text{Mn}^{\text{IV}}(\text{O})(\text{T}_{\text{piv}}\text{PP})]^{2+}$ ^h	6551.2	~6541 ^e	NR ^d	NR ^d	10
$[\text{Mn}^{\text{IV}}(\text{O})(\text{salen})]^+$ ⁱ	6549.9	6538.9	0.046	NR ^d	14
$[\text{Mn}^{\text{IV}}(\text{OH})(\text{salen})]^{+}$ ⁱ	6549.9	6539.0	0.044	NR ^d	14

^aTo permit comparison to the peak heights reported for other $\text{Mn}^{\text{IV}}-\text{OH}$ and $\text{Mn}^{\text{IV}}=\text{O}$ complexes, we have normalized each XANES spectrum with respect to the most intense fluorescence peak (see Figure 4). ^bExperimental areas have been multiplied by 100. ^cThis work. ^dNR = not reported. ^eThe pre-edge feature for this complex was reported as being “some 10 eV lower in energy than the edge”; see ref 10. ^fFrozen $\text{CF}_3\text{CH}_2\text{OH}$ solution collected at NSLS I (Brookhaven National Lab). ^gFrozen $\text{CF}_3\text{CH}_2\text{OH}$ solution collected at Advanced Photon Source (Argonne National Lab). ^hFrozen THF/DMF solution collected at Synchrotron Radiation Source (Daresbury Laboratory). ⁱFrozen $\text{CH}_3\text{CH}_2\text{CN}$ solutions collected at Super Photon Ring -8 GeV (Spring-8; Japan).

Scheme 1. Molecular Structures of Oxo- and Hydroxo-manganese(IV) Complexes^a



^aThese structures are inferred on the basis of spectroscopic data and, in some cases, from models developed using DFT methods.

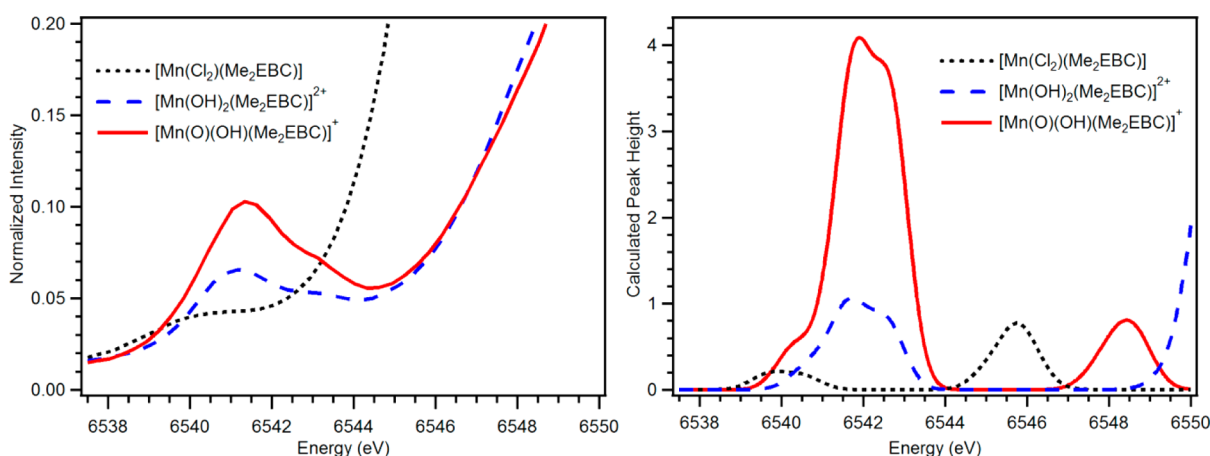


Figure 5. Experimental (left) and calculated (right) pre-edge regions of 1 (black, dotted line), 2 (blue, dashed line), and 3 (red, solid line). For the calculated spectra, a 32.6 eV energy shift and 1 eV Gaussian broadening were applied.

distances obtained from DFT-optimized models are in excellent agreement with those determined experimentally (Table 2). TD-DFT calculations were performed using DFT-optimized models of 1, 2, and 3. (Separate TD-DFT calculations using a model derived directly from XRD coordinates for 2 showed

only minor differences when using XRD- versus DFT-derived models; see Figure S4.) The calculated pre-edge spectra are compared to the corresponding experimental pre-edge spectra in Figure 5 (right and left, respectively). The pre-edge properties are summarized in Table 4. Using a previously

Table 4. Experimental and Calculated Pre-edge Energies (eV), Heights, Areas, Calculated Mn 4p Character in Acceptor MOs, and Mn=O and Mn–OH Distances

complex	experimental ^a			calculated				
	pre-edge energy	height	area ^b	pre-edge energy ^c	intensity ^d	area ^d	Mn 4p (%) ^f	distance Mn–O(H)
[Mn ^{II} (Cl ₂)(Me ₂ EBC)]	6540.4	0.041	3.9	6540.2	0.12	2.5	0.7	
[Mn ^{IV} (OH) ₂ (Me ₂ EBC)] ²⁺	6541.0	0.066	6.9	6541.7	0.66	5.8	1.5	1.814 ^e
[Mn ^{IV} (O)(OH)(Me ₂ EBC)] ⁺	6543.2	0.052		6542.5				
	6541.2	0.103	14.2	6541.9	2.63	17.6	6.9	1.680
	6543.3	0.072		6542.6				1.834 ^e
[Mn ^{IV} (O)(N4py)] ^{2+g}	6541.9	0.077	12.7	6542.4	2.21	15.1	5.4	1.673
[Mn ^{IV} (O)(Bn-TPEN)] ^{2+h}	6541.6	NR	NR	6542.3	2.24	15.2	4.0	1.678
[Mn ^{IV} (O)(T _{piv} PP)] ⁱ	~6541	NR	NR	6542.0	4.33	27.8	19.9	1.662
[Mn ^{IV} (O)(salen)] ^j	6538.9	0.046	NR	6541.9	4.13	26.6	11.7	1.670
[Mn ^{IV} (OH)(salen)] ^{kj}	6539.0	0.044	NR	6541.4	1.69	11.9	6.8	1.810 ^e
[Mn ^{IV} (O)(salen)(C ₃ H ₅ N)]				6542.3	3.05	20.1	3.3	1.675
[Mn ^{IV} (OH)(salen)(C ₃ H ₅ N)] ⁺				6541.5	0.87	7.0	1.8	1.818 ^e
				6542.3				
[Mn ^{IV} (O)(H ₃ buea)] ⁻				6541.3	2.62	17.5	13.5	1.715
				6542.3				
[Mn ^V (O)(H ₃ buea)]				6541.3	3.18	20.9	13.1	1.696
				6542.8				

^aTo permit comparison to the calculated peak heights, each XANES spectrum is normalized with respect to the most intense fluorescence peak (see Figure 4). ^bTotal pre-edge area multiplied by 100. ^cThe calculated energy includes a 32.6 eV shift. ^dThe calculated intensity and area determined as described in the experimental section and Supporting Information. ^eMn–OH distance. ^fRepresents the sum of Mn 4p (%) for all of the acceptor MOs contributing to the transitions within the pre-edge envelope. ^gExperimental data from ref 15. ^hExperimental data from ref 16. ⁱExperimental data from ref 10. ^jExperimental data from ref 14.

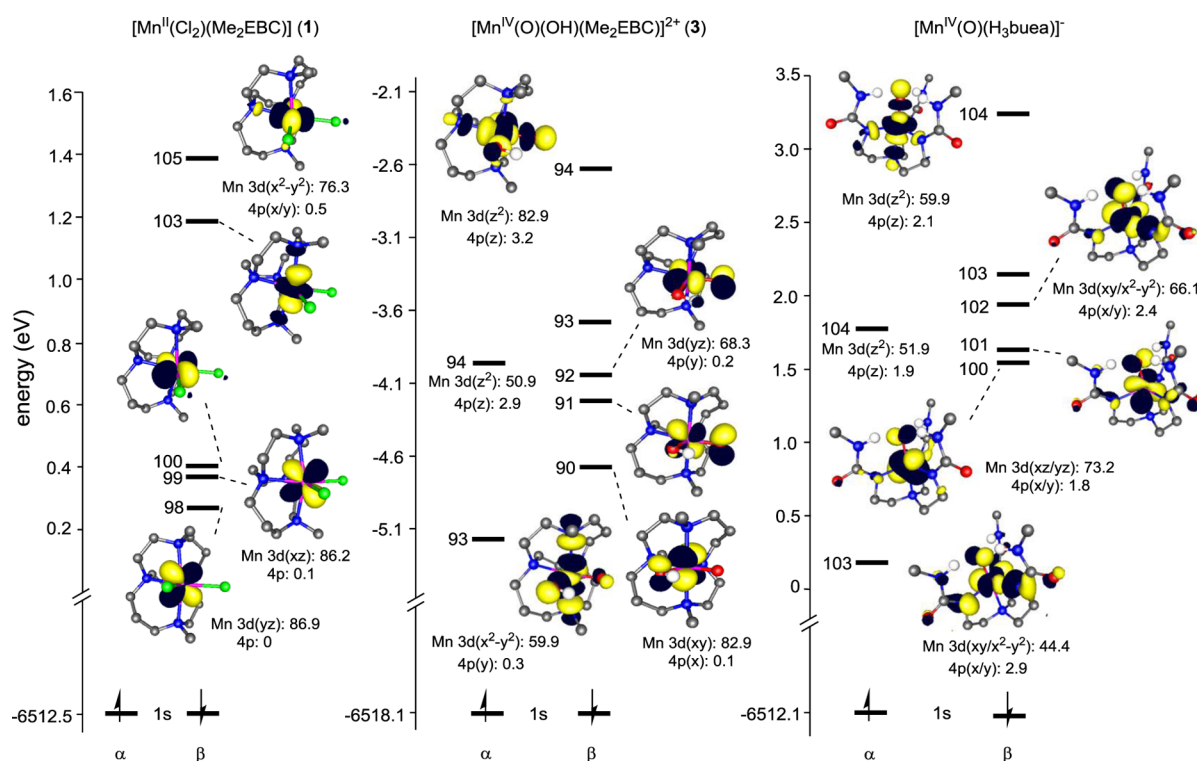


Figure 6. MO diagram of [Mn^{II}(Cl₂)(Me₂EBC)] (1), [Mn^{IV}(O)(OH)(Me₂EBC)]²⁺ (3), and [Mn^{IV}(O)(H₃buea)]⁻. The energies are for the spin unrestricted Kohn–Sham orbitals. The representative surface contour plots for individual Kohn–Sham 3d-based orbitals are given, with the dominant Mn 3d and 4p contributors in parentheses.

described protocol, the calculated spectra were shifted 32.6 eV to higher energy to correct for systematic errors in the level of theory (i.e., density functional, basis set, etc.).³⁴ For all three complexes, the TD-DFT-calculated pre-edge spectra consist of two features (Figure 5, right). The bands at lower energy

(~6539–6544 eV) correspond to pre-edge Mn 1s-to-3d transitions. The bands above 6544 eV arise from metal-to-ligand charge-transfer (MLCT) transitions. In the experimental spectra, the MLCT transitions are often concealed within the rising edge, and, therefore, experimental energies are difficult to

Table 5. Manganese-Ligand Bond Lengths (Å) for DFT-Optimized Models of Mn^{IV}=O and Mn^{IV}-OH Complexes

complex	Mn–O(H) ^a	Mn–N _{eq} ^{a,b}	Mn–N _{ax} ^{a,c}	Mn–O ^{a,d}	ref
[Mn ^{IV} (O)(N4py)] ²⁺	1.673 (1.69)	2.02 (2.00)	2.14 (2.24)		15
[Mn ^{IV} (O)(Bn-TPEN)] ²⁺	1.678 (1.69)	2.07 (2.04)	2.19 (2.40)		16
[Mn ^{IV} (O)(T _{piv} PP)]	1.662 (1.69)	2.01 (2.00)			10
[Mn ^{IV} (O)(salen)]	1.670 (1.58)	1.99 (1.99)		1.90 (1.81)	14
[Mn ^{IV} (O)(salen)(CH ₃ CH ₂ CN)]	1.675	1.96	2.31	1.93	
[Mn ^{IV} (OH)(salen)] ⁺	1.810 (1.83) ^e	1.98 (1.98)		1.85 (1.83)	14
[Mn ^{IV} (OH)(salen)(CH ₃ CH ₂ CN)] ⁺	1.818 ^e	1.99	2.13	1.87	
[Mn ^{IV} (O)(H ₃ buea)] ⁻	1.715	1.98	2.17		
[Mn ^V (O)(H ₃ buea)]	1.696	1.89	2.13		

^aDistances determined from analysis of EXAFS data are provided in parentheses. ^bAverage Mn–N_{eq} (equatorial) distance. ^cMn–N_{ax} (axial) distance. ^dAverage Mn–O (phenolate) distance. ^eMn^{IV}–OH distance.

determine. Furthermore, the calculated energy for these transitions are highly dependent on the percentage of Hartree–Fock (HF) exchange incorporated into the density functional.³⁴ On the basis of these considerations, the MLCT transitions will not be addressed further.

As the oxidation state of the Mn ion increased from +2 in **1** to +4 in **2** and **3**, the calculated pre-edge energies for **2** and **3** (6541.7 and 6541.9 eV, respectively) blue-shift relative to that of **1** (6540.2 eV). However, the TD-DFT calculations for **2** and **3** overestimated the energy of the dominant pre-edge transition by 0.7 eV compared to experiment (Figure 5 and Table 4). In contrast, the experimental pre-edge areas of **2** and **3** (6.9 and 14.2, respectively) are in excellent absolute agreement with the calculated areas (5.8 and 17.6, respectively; Table 4), although the calculated intensity ratio for the pre-edge of **3** to **2** is overestimated (calculated and experimental ratios are 4:1 and 2:1, respectively). A broader pre-edge peak is calculated for **3**, consistent with the experimental observation (Figure 5). Overall, the TD-DFT-calculated spectra are in good agreement with the experimental data. Given that the TD-DFT computations successfully reproduce the pre-edge properties of **1**, **2**, and **3**, it is warranted to use these calculations to more rigorously assign the pre-edge features of these complexes.

(B). Spectral Assignments for the Pre-Edge Region of 1. The electronic transitions contributing to the pre-edge feature in **1** can be well-understood by examining the Mn 3d orbital splitting pattern shown in Figure 6 (left). Because **1** is high-spin ($S = 5/2$) and of low symmetry, 1s-to-3d XAS transitions will originate in the 1s β -spin orbital and terminate in one of the five 3d β -spin orbitals, in each case giving a $(1s)^1(3d)^6$ excited configuration. Thus, five excited states can potentially contribute to the pre-edge region. As shown in Figure 6 (left), the β -spin 3d manifold of **1** is split in a pseudo-octahedral fashion, with the t_{2g} -type orbitals (98β , 99β , and 100β) approximately 1 eV below the e_g -type orbitals (103β and 105β). The 1 eV splitting of the t_{2g} - and e_g -derived orbitals is comparable to the $10Dq$ values of $[\text{Mn}^{\text{II}}(\text{L})_6]^{n+}$ complexes with weak- to moderate-field ligands ($\text{L} = \text{Cl}^-$, H_2O , or ethylenediamine; 0.93, 1.05, 1.25 eV, respectively).⁶⁹ In the TD-DFT calculations, the pre-edge feature at ~ 6540.2 eV reflects the 3d orbital splitting pattern (Figure 5, right). Specifically, there are a set of three transitions at lower energy, contributing to the shoulder at 6539.7 eV (Figure S5, Supporting Information), that correspond to excitations into the unoccupied t_{2g} -derived orbitals (98β , 99β , and 100β). A set of two transitions at higher energy (6540.5 eV) arise from excitations into the unoccupied e_g -derived orbitals (103β and 105β). Together, the five acceptor molecular orbitals (MOs) contain <1% total Mn 4p

character (Table 4). Thus, the pre-edge transitions gain only modest dipole-allowed intensity from Mn 3d–4p orbital mixing. The TD-DFT calculations provide excellent support for the assignment that the pre-edge intensity in **1** arises predominantly from the electric-quadrupole mechanism.

(C). Spectral Assignments for the Pre-Edge Regions of 2 and 3. The 3d-orbital splitting patterns of **2** and **3** were discussed previously within the context of MCD investigations of these complexes.¹⁸ Those results will be briefly summarized here to provide a framework for understanding the pre-edge data. Both **2** and **3** are high-spin ($S = 3/2$). Thus, the e_g -derived α -spin orbitals (93α and 94α for both **2** and **3**), and all β -spin Mn 3d-based orbitals, are unoccupied (see Figure 6, center, for the Mn 3d orbital splitting for **3**). The e_g -derived MOs are split considerably in both complexes. For **2**, the $3d_{xy}$ MO, which is σ -antibonding with both hydroxide ligands, is highest in energy (in this complex, the y -axis bisects the HO–Mn–OH angle).¹⁸ For **3**, a strong σ -antibonding interaction with the oxo ligand along the z -axis (the Mn=O vector) pushes the $3d_z^2$ MO above the $3d_{x^2-y^2}$ MO (Figure 6, center). Complex **3** also displays a larger splitting of the t_{2g} -derived MOs compared to **2**, which reflects the strong π -donating properties of the oxo ligand. For both complexes, the α -spin (majority spin) Mn 3d orbitals are stabilized by ~ 1.3 – 1.9 eV relative to their β -spin counterparts because of spin polarization due to electron exchange.

For the dihydroxo complex **2**, excitations of Mn 1s- α and 1s- β electrons into the respective α - and β - $3d_{xy}$ orbitals (94α and 94β) contribute $\sim 80\%$ of the intensity of the pre-edge feature. These transitions are split by 1 eV (6541.6 and 6542.6 eV, respectively) due to the exchange stabilization of the α -spin manifold. The pre-edge feature of **2** gains additional intensity (<20%) from excitations into the α - and β - $3d_z^2$ orbitals at 6541.1 and 6541.8 eV, respectively (93α and 93β). Excitations terminating in the $3d_{xy}$ MOs are more intense because of the higher percentage of Mn 4p character in the $3d_{xy}$ MOs (1.2%) than the $3d_z^2$ MOs (0.3%). This increased mixing renders the calculated oscillator strengths for the transitions into the $3d_{xy}$ orbitals an order of magnitude greater than those involving the $3d_z^2$ orbitals (Table S2, Supporting Information). The low-energy shoulder in the pre-edge feature of **2** (Figure 5, right) arises from three weak transitions corresponding to excitations into the unoccupied β - $3d_{xz}$, $3d_{yz}$, and $3d_{xy}$ orbitals that contain minimal 4p character (<0.1%).

For the oxohydroxo complex **3**, the pre-edge feature derives $\sim 90\%$ of its intensity from two transitions into the unoccupied α - and β - $3d_z^2$ orbitals (6541.8 and 6542.7 eV, respectively). The acceptor orbitals (94α and β) contain a relatively large

admixture of Mn 4p character (6.1%), giving significant dipole-allowed intensity. This accounts for the calculated pre-edge intensity of 3 being nearly four times that of 2 (Table 4).

In summary, the different pre-edge properties of 2 and 3 can be directly understood on the basis of 4p-mixing into the respective Mn–OH ($3d_{xy}$) and Mn=O ($3d_z$) orbitals. Only minor (<20%) pre-edge intensity derives from excitations into Mn π -type MOs. To determine how these specific results are affected by perturbations in ligand type, as well as the geometry of the Mn center, we extended our computational investigations to a series of Mn^{IV}=O and Mn^{IV}–OH complexes (Scheme 1).

(D). *TD-DFT Mn Pre-edge Calculations for Other Mn^{IV}=O and Mn^{IV}–OH Complexes. General Considerations.* DFT calculations were used to obtain structural models of [Mn^{IV}(O)(N4py)]²⁺ and [Mn^{IV}(O)(Bn-TPEN)]²⁺ (six-coordinate);^{15,16} [Mn^{IV}(O)(salen)], [Mn^{IV}(OH)(salen)]⁺, and [Mn^{IV}(O)(T_{piv}PP)] (five-coordinate, square pyramidal);^{10,14} and [Mn^{IV}(O)(H₃buea)]⁻ (five-coordinate, trigonal bipyramidal).²⁰ Although no crystal structures are available for comparison, EXAFS distances have been reported for the majority of these complexes.^{10,14–16} With few exceptions, the DFT-computed metric parameters are in excellent agreement with the experimental distances (Tables 5 and S3). The most egregious deviation between experiment and theory is the Mn^{IV}=O distance of [Mn^{IV}(O)(salen)]; the DFT-computed distance of 1.670 Å is significantly longer than the 1.58 Å obtained from EXAFS analysis.¹⁴ The 1.58 Å EXAFS distance for [Mn^{IV}(O)(salen)] is more consistent with a tetragonal oxomanganese(V) unit (1.55–1.56 Å from X-ray crystallographic and EXAFS studies),^{23–26,35} and it is hard to reconcile this exceptionally short bond length with both the computational result and the range of EXAFS distances for other oxomanganese(IV) species (1.69–1.71 Å; see Tables 5 and 2). We note that previous studies have shown that the DFT level of theory used here is quite accurate for the short M=O distances of high-valent metal-oxo species.^{40,70,71} Therefore, in our discussion of the pre-edge properties of [Mn^{IV}(O)(salen)], we assume that the DFT distance is reliable.

TD-DFT-computed pre-edge properties for all five complexes are shown in Figure 7 and summarized in Table 4. Some general trends can be immediately noted. All calculated pre-edge energies are in good agreement with the experimental values; most deviations are less than 1 eV. Larger deviations are observed for the [Mn^{IV}(O)(salen)] and [Mn^{IV}(OH)(salen)]⁺ complexes, but this could be related to the different energy calibration protocol used for these complexes (*vide supra*). With regard to pre-edge intensity, the most intense features are predicted for [Mn^{IV}(O)(salen)] and [Mn^{IV}(O)(T_{piv}PP)]. This is expected, given that the lack of a ligand *trans* to the oxo in these square pyramidal complexes introduces a large deviation from centrosymmetry along this axis. The complexes [Mn^{IV}(O)(N4py)]²⁺, [Mn^{IV}(O)(Bn-TPEN)]²⁺, and [Mn^{IV}(O)(H₃buea)]⁻ all have similar peak heights (Table 4), although the last complex shows a much broader pre-edge envelope, and, therefore, a greater pre-edge area (Figure 7). Finally, the Mn^{IV}–OH complex [Mn^{IV}(OH)(salen)]⁺ displays the smallest pre-edge peak area.

(E). *Spectral Assignments for the Pre-Edge Spectra of [Mn^{IV}(O)(T_{piv}PP)] and [Mn^{IV}(O)(salen)].* The calculated pre-edge intensities for the square pyramidal [Mn^{IV}(O)(T_{piv}PP)] and [Mn^{IV}(O)(salen)] complexes arise predominantly (>90%) from excitations into the α - and β - $3d_z$ orbitals (Mn^{IV}=O σ^*

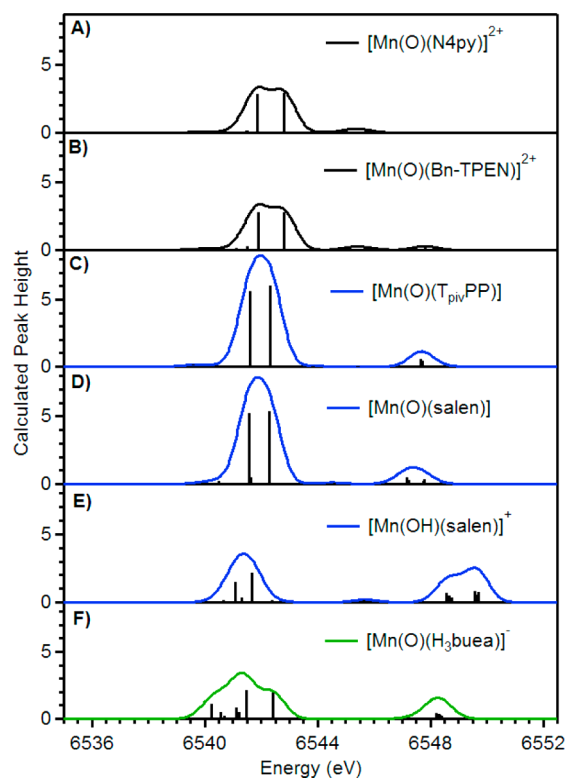


Figure 7. TD-DFT calculated pre-edge spectra for (A) [Mn^{IV}(O)(N4py)]²⁺, (B) [Mn^{IV}(O)(Bn-TPEN)]²⁺, (C) [Mn^{IV}(O)(T_{piv}PP)], (D) [Mn^{IV}(O)(salen)], (E) [Mn^{IV}(OH)(salen)]⁺, and (F) [Mn^{IV}(O)(H₃buea)]⁻. Sticks mark individual electronic transitions. Note that the same y-scale is used for all plots.

MOs). These acceptor MOs contain 11–20% Mn 4p character (Table 4). The lack of pseudoinversion symmetry along the Mn=O axis greatly increases $3d_z$ - $4p_z$ mixing, and, thus, pre-edge intensity. Consequently, [Mn^{IV}(O)(T_{piv}PP)] and [Mn^{IV}(O)(salen)] show a nearly 2-fold increase in pre-edge height compared to six-coordinate oxomanganese(IV) complexes (Figure 7), which arises from an increase in $3d$ - $4p$ mixing by a factor of 2–3 (Table 4).

(F). *Spectral Assignments for the Pre-Edge Spectra of [Mn^{IV}(O)(N4py)]²⁺ and [Mn^{IV}(O)(Bn-TPEN)]²⁺.* The calculated pre-edge features of [Mn^{IV}(O)(N4py)]²⁺ and [Mn^{IV}(O)(Bn-TPEN)]²⁺ are at higher energy, and with lower intensity, than that of 3, fully consistent with the experimental data (Table 4).^{15,16} For both [Mn^{IV}(O)(N4py)]²⁺ and [Mn^{IV}(O)(Bn-TPEN)]²⁺, the Mn $3d_z$ MO is highest in energy due to a strong σ -antibonding interaction with the oxo ligand. Similar to the other oxomanganese(IV) complexes, excitations into the unoccupied α - and β - $3d_z$ orbitals (Mn^{IV}=O σ^* MOs) give rise to two dominant transitions split by 0.9 eV that contribute >90% of the intensity to the pre-edge feature (Table S4, Supporting Information). The acceptor $3d_z$ orbitals for [Mn^{IV}(O)(N4py)]²⁺ contain a smaller admixture of Mn 4p character than 3 (5.4 and 6.9%, respectively), consistent with the lower experimental pre-edge peak height of [Mn^{IV}(O)(N4py)]²⁺ than that of 3 (0.077 and 0.103, respectively; Table 4). The pre-edge intensity for [Mn^{IV}(O)(Bn-TPEN)]²⁺ was not reported and thus cannot be compared here.¹⁶

(G). *Spectral Assignments for the Pre-Edge Spectra of [Mn^{IV}(O)(H₃buea)]⁻.* Although XAS data have not been reported for [Mn^{IV}(O)(H₃buea)]⁻, its inclusion in our

computational investigations is important, as this complex represents a rare example of a $\text{Mn}^{\text{IV}}=\text{O}$ unit in a trigonal bipyramidal geometry. This geometry gives rise to a Mn 3d orbital splitting pattern distinct from that of **3** and other $\text{Mn}^{\text{IV}}=\text{O}$ units in an octahedral or square pyramidal geometry. The DFT-derived 3d MO splitting pattern for $[\text{Mn}^{\text{IV}}(\text{O})(\text{H}_3\text{buea})]^-$ shows a deviation from that expected for a complex with idealized C_{3v} symmetry (Figure 6, right). In this idealized geometry, the $3d_z^2$ orbital ($\text{Mn}^{\text{IV}}=\text{O} \sigma^*$ MO; 104β) would lie above two sets of e -type orbitals: $3d_{x^2-y^2}$, $3d_{xy}$ ($\text{Mn}^{\text{IV}}-\text{N}_{\text{eq}} \sigma^*$; 103β and 102β); and $3d_{xz}$, $3d_{yz}$ ($\text{Mn}^{\text{IV}}=\text{O} \pi^*$; 101β and 100β). For an $S = 3/2$ system such as $[\text{Mn}^{\text{IV}}(\text{O})(\text{H}_3\text{buea})]^-$, this splitting would give a Jahn–Teller active 4E ground state, which arises from the $(e)^2(e)^1$ electron configuration. Jahn–Teller distortions are noted in the asymmetric $\text{Mn}^{\text{IV}}-\text{N}_{\text{eq}}$ bond lengths and $\text{N}_{\text{eq}}-\text{Mn}^{\text{IV}}-\text{N}_{\text{eq}}$ angles in the DFT model of $[\text{Mn}^{\text{IV}}(\text{O})(\text{H}_3\text{buea})]^-$ (Table S6, Supporting Information). Inequivalent $\text{Mn}^{\text{IV}}-\text{N}_{\text{eq}}$ bond lengths and $\text{N}_{\text{eq}}-\text{Mn}^{\text{IV}}-\text{N}_{\text{eq}}$ angles were also evident in a previously described DFT structure of $[\text{Mn}^{\text{IV}}(\text{O})(\text{H}_3\text{buea})]^-$.²⁰ These distortions break the degeneracy of two sets of e orbitals, as shown in Figure 6 (right). In addition, mixing of the parent e orbitals leads to a small amount of oxo π -character in the $3d_{x^2-y^2}$ and $3d_{xy}$ MOs (103β and 102β).

This bonding pattern, which is distinct from that of **3** (Figure 6, center), leads to a pre-edge spectrum broader than those of octahedral or square pyramidal $\text{Mn}^{\text{IV}}=\text{O}$ compounds (Figure 7). The pre-edge spectra of those complexes are completely dominated by excitations terminating in the α - and β - $3d_z^2$ orbitals ($\text{Mn}^{\text{IV}}=\text{O} \sigma^*$). These excitations are split by 0.9 eV, which defines the width of the pre-edge feature. For $[\text{Mn}^{\text{IV}}(\text{O})(\text{H}_3\text{buea})]^-$, the TD-DFT calculations predict a broad (~ 3 eV) pre-edge feature with intense peaks at 6541.3 and 6542.3 eV, and a shoulder at 6540.2 eV (Figure 7F and Table 4). The two peaks at highest energy correspond to excitations to the α - and β - $3d_z^2$ orbitals (104α and 104β ; $\text{Mn}^{\text{IV}}=\text{O} \sigma^*$) that contain 4% total Mn 4p character. The shoulder at 6540.2 eV arises from a transition terminating in the α - $3d_{x^2-y^2}$ MO (103α) that contains 2.9% Mn 4p character. Although there is less Mn 4p character in the α - and β - $3d_z^2$ orbitals in $[\text{Mn}^{\text{IV}}(\text{O})(\text{H}_3\text{buea})]^-$ than in six-coordinate oxomanganese(IV) complexes, the trigonal symmetry allows for 4p_{xy} mixing into the $3d_{xy}$ and $3d_{x^2-y^2}$ orbitals. Thus, the broader pre-edge feature of $[\text{Mn}^{\text{IV}}(\text{O})(\text{H}_3\text{buea})]^-$ is due to the presence of excitations terminating in the $3d_{xy}$ and $3d_{x^2-y^2}$ orbitals, which gain electric dipole character and cause a distribution of pre-edge intensity over a larger number of transitions that span a wider range of energy. Importantly, the related Fe^{III} complex, $[\text{Fe}^{\text{III}}(\text{O})(\text{H}_3\text{buea})]^{2-}$, shows a broad pre-edge feature (~ 3 eV) in the experimental Fe pre-K-edge spectrum that is likely of similar origin.⁵⁵

DISCUSSION

Mn K-edge XAS has been used for decades to aid in the characterization of biological and synthetic manganese complexes. In particular, this technique has played a critical role in defining manganese-ligand distances for oxomanganese(IV) complexes that have eluded characterization by X-ray crystallography.^{10,12–16} In this study, Mn K-edge XAS was used to determine metric parameters and to explore the pre-edge properties of a manganese(II) and two manganese(IV) complexes supported by the tetradentate Me_2EBC ligand. Specifically, the first structural data for $[\text{Mn}^{\text{IV}}(\text{O})(\text{OH})-$

$(\text{Me}_2\text{EBC})]^{+}$ (**3**) were obtained from EXAFS fits. This analysis revealed a Mn=O distance of 1.71 Å and a Mn–OH distance of 1.84 Å, in excellent agreement with the previously reported DFT structure.¹⁸ Thus, these data permit the unambiguous identification of this species as a rare example of an oxohydroxomanganese(IV) complex, corroborating previous assignments.^{18,22,27} This work also allowed for a direct structural and pre-edge comparison between $\text{Mn}^{\text{IV}}=\text{O}$ and $\text{Mn}^{\text{IV}}-\text{OH}$ adducts (**2** and **3**, respectively) that differ by only a proton. TD-DFT calculations reveal that the different pre-edge properties of **2** and **3** can be directly understood on the basis of 4p-mixing into the Mn $3d_{xy}$ and $3d_z^2$ orbitals, respectively, that reflect the dominant hydroxo- and oxo-manganese σ -interactions. In contrast, the intensity of the weak pre-edge peak of the manganese(II) complex **1** derives predominantly from electric-quadrupole allowed 1s-to-3d transitions (74%). Minor Mn 3d-4p mixing in **1** introduces a 20% contribution from the electric-dipole intensity mechanism to the pre-edge envelope (Table S8, Supporting Information).

Because our primary concern in this present study is to define the impact of the ligand environment (i.e., identity and effective symmetry of the ligand sphere) on the pre-edge properties of mononuclear manganese(IV) complexes, the TD-DFT methodology appeared most appropriate. This approach has the advantage that the calculated pre-edge properties can be related to commonplace chemical concepts such as MOs. However, the TD-DFT method is not without its limitations. For example, 3d-3d multiplet effects are not explicitly accounted for, but are only approximated to some extent through spin-polarization effects.^{29,44,72} Alternative approaches to calculate pre-edge properties, which include *ab initio* FEFF and ligand-field multiplet calculations, have shown success for manganese systems.^{73,74} The ligand-field multiplet method explicitly incorporates multiplet effects; however, application of this approach often focuses solely on quadrupole-intensity mechanisms. Furthermore, the impact of the coordination sphere is approximated through standardized ligand-field parameters (i.e., $10Dq$), so that it is challenging to incorporate subtle changes in ligand donor strength and/or metal–ligand covalency. A multiple-scattering FEFF method using a muffin tin potential was shown to be very powerful in reproducing the pre-edge features of a series of manganese oxide compounds.⁷³ In particular, this work highlighted the importance of longer-range metal–metal transitions in understanding the pre-edge properties of polymeric metal oxides. It is, however, difficult to relate the FEFF results to the orbital concepts so familiar to chemists.

Correlation between Pre-Edge Properties and Geometric Structure for $\text{Mn}^{\text{IV}}=\text{O}$ and $\text{Mn}^{\text{IV}}-\text{OH}$ Complexes.

Oxomanganese(IV) complexes exhibit moderately intense pre-edge features that have been qualitatively linked to short Mn=O distances that range from 1.67 to 1.71 Å.^{12–14} This trend is illustrated in Figure 8 (top), where the TD-DFT-calculated pre-edge areas are compared with the DFT-calculated Mn–O distances of $\text{Mn}^{\text{IV}}=\text{O}$ and $\text{Mn}^{\text{IV}}-\text{OH}$ complexes. In general, the calculated pre-edge areas decrease as the Mn–O distance increases. The spectral assignments afforded by the TD-DFT computations provide insights into the basis for this correlation. The pre-edge features of oxomanganese(IV) complexes are dominated by excitations to the Mn=O σ^* MOs (the Mn $3d_z^2$ MOs), as these orbitals contain an appreciable admixture of Mn 4p character. However, the extent of 3d-4p mixing is modulated by both the Mn=O (or $\text{Mn}^{\text{IV}}-\text{OH}$) distance and the Mn

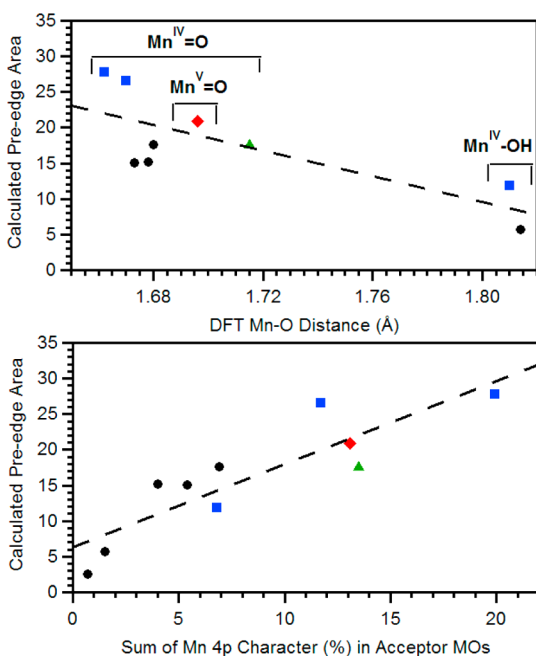


Figure 8. Calculated pre-edge area as a function of Mn–O distance in the DFT-optimized structures (top) and of the total Mn 4p character in the acceptor MOs for the electronic transitions within the pre-edge peak (bottom, see Table 4). Black circles mark data for **1**, **2**, **3**, $[\text{Mn}^{\text{IV}}(\text{O})(\text{N4py})]^{2+}$, and $[\text{Mn}^{\text{IV}}(\text{O})(\text{Bn-TPEN})]^{2+}$; blue squares mark data for $[\text{Mn}^{\text{IV}}(\text{O})(\text{salen})]$, $[\text{Mn}^{\text{IV}}(\text{OH})(\text{salen})]^+$, and $[\text{Mn}^{\text{IV}}(\text{O})(\text{T}_{\text{piv}}\text{PP})]$; the green triangle marks data for $[\text{Mn}^{\text{IV}}(\text{O})(\text{H}_3\text{buea})]^-$; and the red diamond marks data for $[\text{Mn}^{\text{V}}(\text{O})(\text{H}_3\text{buea})]$.

coordination geometry. Thus, a better correlation is observed between the calculated pre-edge area and the sum of Mn 4p character (%) in all acceptor MOs (Figure 8, bottom), as the latter parameter is reflective of the entire Mn^{IV} ligand field and not just the Mn–O distance. Two points of comparison well-illustrate this point. First, for both oxo- and hydroxomanganese(IV) adducts, the calculated pre-edge area of square pyramidal complexes (blue squares, Figure 8, top) is roughly a factor of 2 greater than that of six-coordinate complexes with similar Mn–O distances (black circles, Figure 8, top). This is because the greatest Mn 3d_{z²}-4p_z mixing is observed for the square pyramidal complexes that lack a ligand *trans* to the oxo. Second, the calculated pre-edge area of a square pyramidal Mn^{IV}-OH adduct (11.9) is only slightly lower than that of pseudo-octahedral Mn^{IV}=O adducts (15.1–17.6). On the basis of these comparisons, the assignment of Mn^{IV}-OH versus Mn^{IV}=O motifs using pre-edge data alone is not advisable.

Importantly, the Mn^{IV} geometry also influences the breadth of the pre-edge feature. For the six-coordinate oxomanganese(IV) complexes, the energy splitting of the dominant calculated pre-edge transitions are around 1 eV and reflect the exchange stabilization of the majority-spin orbitals relative to their minority-spin counterparts. In contrast, the trigonal bipyramidal oxomanganese(IV) complex $[\text{Mn}^{\text{IV}}(\text{O})(\text{H}_3\text{buea})]^-$ shows a pre-edge peak with an area similar to that of the six-coordinate oxomanganese(IV) complexes, but with an energy splitting of the dominant calculated pre-edge transitions of around 3 eV. This is because $[\text{Mn}^{\text{IV}}(\text{O})(\text{H}_3\text{buea})]^-$ displays total 3d-4p mixing on par with that of the square pyramidal complexes; however, the 4p character is more evenly distributed throughout the 3d manifold. Although experimental pre-edge data for a trigonal bipyramidal oxomanganese(IV) complex

have not yet been reported, our computations predict such a species could be expected to show a pre-edge area similar to that of square pyramidal Mn^{IV}=O complexes, but with a smaller pre-edge height. These considerations highlight the importance of reporting pre-edge area, and not height of pre-edge maxima, when comparing pre-edge features of different complexes.

Pre-Edge Energies and Intensities: Experiment versus Theory. In general, the experimental pre-edge properties for the nine Mn^{IV} complexes investigated in this study are well reproduced by a TD-DFT method initially calibrated using a large test set of Mn(II) and Mn(III) complexes.³⁴ To better judge the success of this correlation in the present case, experimental and calculated pre-edge peak energies and areas are compared in Figures 9 and 10, respectively. A linear

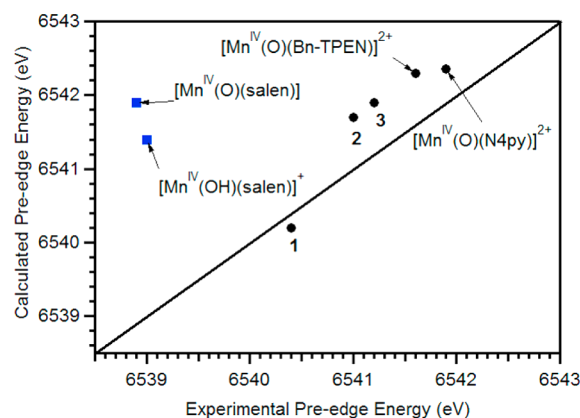


Figure 9. Correlation between the calculated pre-edge energy (with the +32.6 eV energy correction) and the experimental pre-edge energy for $[\text{Mn}^{\text{II}}(\text{Cl}_2)(\text{Me}_3\text{EBC})]$ (**1**), $[\text{Mn}^{\text{IV}}(\text{OH})_2(\text{Me}_3\text{EBC})]^{2+}$ (**2**), $[\text{Mn}^{\text{IV}}(\text{O})(\text{OH})(\text{Me}_3\text{EBC})]^+$ (**3**), $[\text{Mn}^{\text{IV}}(\text{O})(\text{N4py})]^{2+}$, $[\text{Mn}^{\text{IV}}(\text{O})(\text{Bn-TPEN})]^{2+}$, $[\text{Mn}^{\text{IV}}(\text{O})(\text{salen})]$ and $[\text{Mn}^{\text{IV}}(\text{OH})(\text{salen})]^+$.

correlation, albeit with some scatter, is observed between the experimental and calculated pre-edge energies of **1**, **2**, **3**, $[\text{Mn}^{\text{IV}}(\text{O})(\text{N4py})]^{2+}$, and $[\text{Mn}^{\text{IV}}(\text{O})(\text{Bn-TPEN})]^{2+}$. The calculated pre-edge energies for **2**, **3**, $[\text{Mn}^{\text{IV}}(\text{O})(\text{N4py})]^{2+}$, and $[\text{Mn}^{\text{IV}}(\text{O})(\text{Bn-TPEN})]^{2+}$ are systematically overestimated by approximately 0.5 eV relative to experiment (Figure 9 and Table 4). The $[\text{Mn}^{\text{IV}}(\text{O})(\text{salen})]$ and $[\text{Mn}^{\text{IV}}(\text{OH})(\text{salen})]^+$ complexes are large outliers to this trend, as the experimental energies are nearly 2 eV lower than the theoretical values. The most likely explanation for this deviation is the use of a different method for energy calibration of the XAS data. The $[\text{Mn}^{\text{IV}}(\text{O})(\text{salen})]$ and $[\text{Mn}^{\text{IV}}(\text{OH})(\text{salen})]^+$ samples were calibrated to Cu foil,¹⁴ whereas the other oxomanganese(IV) samples were calibrated either to manganese foil^{10,14,15} or to KMnO_4 powder.¹⁶ An alternate explanation would be that the $[\text{Mn}^{\text{IV}}(\text{O})(\text{salen})]$ and $[\text{Mn}^{\text{IV}}(\text{OH})(\text{salen})]^+$ samples underwent photoreduction during X-ray irradiation.

An excellent correlation, with minimal scatter, is also obtained between the calculated pre-edge areas and experimental areas of **1**, **2**, **3**, and $[\text{Mn}^{\text{IV}}(\text{O})(\text{N4py})]^{2+}$ (Figure 10, top). These are the only compounds examined in this study for which the areas of pre-edge peaks were determined. For other complexes, only pre-edge peak heights were reported.¹⁴ Because of the variable widths of the pre-edge features, the pre-edge area is a far better parameter with which to assess the agreement with experiment. Nonetheless, a linear correlation,

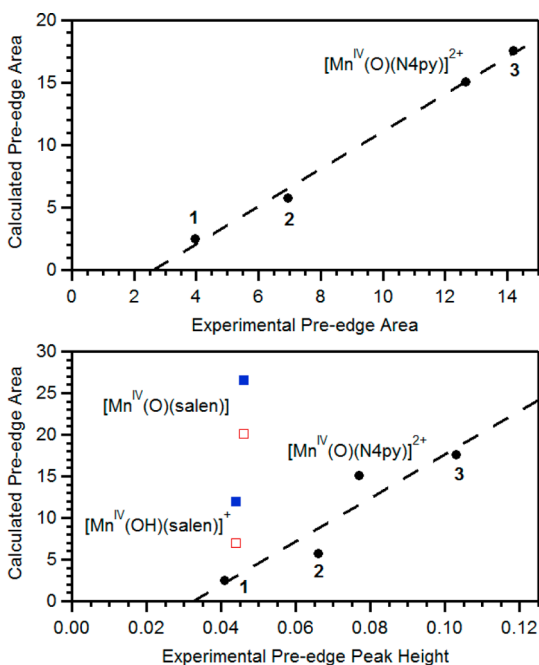


Figure 10. Correlation between the calculated pre-edge area and experimental area of the pre-edge peaks (top) for complexes [Mn^{II}(Cl₂)(Me₂EBC)] (1), [Mn^{IV}(OH)₂(Me₂EBC)]²⁺ (2), [Mn^{IV}(O)(OH)(Me₂EBC)]⁺ (3), and [Mn^{IV}(O)(N4py)]²⁺ and pre-edge peak height (bottom). Also included in bottom panel are model complexes [Mn^{IV}(O)(salen)] (blue solid squares), [Mn^{IV}(OH)(salen)]⁺ (blue solid squares), [Mn^{IV}(O)(salen)(CH₃CH₂CN)] (red open squares), and [Mn^{IV}(OH)(salen)(CH₃CH₂CN)]⁺ (red open squares).

albeit with more scatter, is also observed between the calculated areas and experimental pre-edge peak heights for 1, 2, 3, and [Mn^{IV}(O)(N4py)]²⁺ (Figure 10, bottom). Although the experimental pre-edge peak height for [Mn^{IV}(OH)(salen)]⁺ is low compared to the theoretically predicted value, it is near the border of the scatter of the observed correlation. However, the low experimental height for [Mn^{IV}(O)(salen)] is clearly an outlier.

On the basis of the cumulative experimental and theoretical findings discussed in this work, it is hard to reconcile the small experimental pre-edge intensity of [Mn^{IV}(O)(salen)] with the EXAFS-determined bond length of 1.58 Å, just as it is hard to reconcile this short distance with the DFT-derived model of [Mn^{IV}(O)(salen)] (Table 5). The distance in the DFT-optimized structure (1.670 Å) is consistent with that of other Mn^{IV}=O complexes. In an attempt at reconciliation, we developed additional models of [Mn^{IV}(O)(salen)] and [Mn^{IV}(OH)(salen)]⁺ that included a coordinated solvent ligand (propionitrile, CH₃CH₂CN) *trans* to the oxo. As shown in Figure 10 (red open squares; bottom), and summarized in Table 4, the inclusion of the *trans* solvent ligand lowers the predicted pre-edge areas for both complexes. For [Mn^{IV}(OH)(salen)(CH₃CH₂CN)]⁺, the predicted pre-edge area is now quite consistent with the correlation observed for the other complexes. However, for [Mn^{IV}(O)(salen)(CH₃CH₂CN)], the relationship between the calculated pre-edge area and the experimental pre-edge peak height is still an outlier. In addition, the inclusion of the *trans* solvent ligand leads to a slight elongation in the Mn^{IV}=O bond length (Table 4), rather than a contraction.

Comparison to Oxomanganese(V) Systems. It is useful to frame the results of the present study within the context of high-valent oxomanganese species in general. In particular, the Mn K-edge XANES properties of *S* = 0 oxomanganese(V) adducts have been the subject of several experimental and/or theoretical studies.^{35–38} That work has revealed a strong correlation between pre-edge intensity and coordination geometry.³⁷ For example, square pyramidal oxomanganese(V) species show incredibly intense pre-edges features, much more intense than those of oxomanganese(IV) adducts.³⁶ The absence of such signals during time-resolved XAS studies of the S₃ to S₄ transition of the OEC suggests that a square pyramidal oxomanganese(V) adduct is not involved in water oxidation.⁷⁵ However, as described by Yano and co-workers, reduced Mn 3d-4p mixing in six-coordinate oxomanganese(V) adducts gives rise to much weaker edges when compared to that of their square pyramidal analogues.³⁷ Our present work on oxo- and hydroxomanganese(IV) complexes underscores the conclusions of Yano et al. that “caution must be exercised in using the pre-edge spectrum as an isolated signature of oxidation state”.³⁷

To date, Mn K-edge XAS studies on oxomanganese(V) complexes have been limited to low-spin (*S* = 0) oxomanganese(V) adducts with tetragonal symmetry (i.e., pseudo-octahedral or square pyramidal geometry).^{35–38} Recently, Borovik and co-workers have described the first example of a high-spin (*S* = 1) oxomanganese(V) species, [Mn^V(O)(H₃buea)].⁷⁶ Given that this complex could have considerably different pre-edge properties than its low-spin (*S* = 0) counterparts, we applied the TD-DFT protocol to predict the pre-edge properties of this species.

The DFT-optimized structure of [Mn^V(O)(H₃buea)] displays C_{3v} symmetry, with equivalent Mn^V–N_{eq} distances and N_{eq}–Mn^V–N_{eq} angles of 1.885 Å and 118.35° (Figure 11, right). The Mn^V–N_{eq} bond lengths are reduced considerably compared to the [Mn^{IV}(O)(H₃buea)][–] complex. The Mn 3d orbital splitting diagram of [Mn^V(O)(H₃buea)] (Figure S7, Supporting Information) shows a trigonal ligand-field splitting of the Mn 3d orbitals, confirming the qualitative orbital splitting pattern predicted by Borovik and co-workers.⁷⁶ This splitting

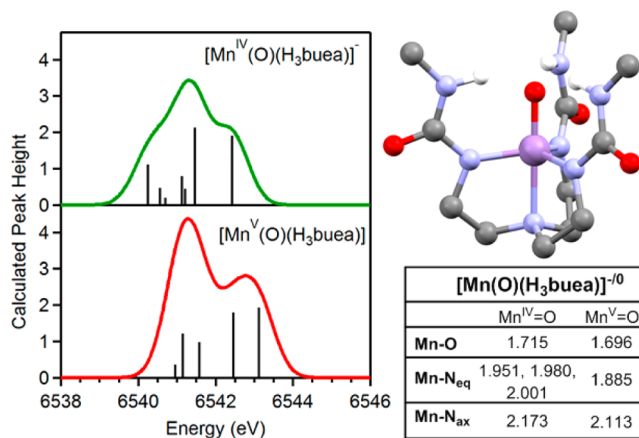


Figure 11. Comparison of TD-DFT calculated pre-edge spectra for [Mn^{IV}(O)(H₃buea)]⁻ (green trace, top) and [Mn^V(O)(H₃buea)] (red trace, bottom). Sticks mark individual electronic transitions. The optimized structure of [Mn^V(O)(H₃buea)], along with the key metric parameters for [Mn^{IV}(O)(H₃buea)]⁻ and [Mn^V(O)(H₃buea)] (Table S6, Supporting Information), are presented on the right.

pattern gives rise to a 3A_2 ground state, from the $(e)^2$ configuration, and thus this complex is not subject to a Jahn–Teller distortion. Importantly, the Mn–oxo distance in $[\text{Mn}^{\text{V}}(\text{O})(\text{H}_3\text{buea})]$ is reduced by less than 0.02 Å compared to that of $[\text{Mn}^{\text{IV}}(\text{O})(\text{H}_3\text{buea})]^-$ (1.696 and 1.715 Å, respectively). The small perturbation in the Mn–oxo distance reflects the fact that the $\text{Mn}=\text{O}$ π^* MOs ($3d_{xz}$ and $3d_{yz}$) are singly occupied in both the $[\text{Mn}^{\text{V}}(\text{O})(\text{H}_3\text{buea})]$ and $[\text{Mn}^{\text{IV}}(\text{O})(\text{H}_3\text{buea})]^-$ complexes.

The calculated pre-edge spectrum of $[\text{Mn}^{\text{V}}(\text{O})(\text{H}_3\text{buea})]$ reveals two pre-edge peaks at 6541.3 and 6542.8 eV (Figure 11, left). The pre-edge maxima for both $[\text{Mn}^{\text{IV}}(\text{O})(\text{H}_3\text{buea})]^-$ and $[\text{Mn}^{\text{V}}(\text{O})(\text{H}_3\text{buea})]$ are calculated to be at 6451.3 eV, despite the higher oxidation state of Mn in $[\text{Mn}^{\text{V}}(\text{O})(\text{H}_3\text{buea})]$. However, the intensity of this band derives from a different set of pre-edge transitions in $[\text{Mn}^{\text{V}}(\text{O})(\text{H}_3\text{buea})]$ than for $[\text{Mn}^{\text{IV}}(\text{O})(\text{H}_3\text{buea})]^-$. For $[\text{Mn}^{\text{IV}}(\text{O})(\text{H}_3\text{buea})]^-$, the intensity of the band at 6541.3 eV derives predominantly from a transition terminating in the α - $3d_z^2$ ($\text{Mn}^{\text{IV}}=\text{O}$ σ^*) MO. In contrast, for $[\text{Mn}^{\text{V}}(\text{O})(\text{H}_3\text{buea})]$, the intense band at 6541.3 eV (~60% overall pre-edge intensity) is composed of three pairs of transitions (split by only 0.6 eV) that cumulatively contribute to the intensity of this feature. The intensity of this band predominantly arises from two pairs of transitions terminating in the degenerate α - $3d_{xy}$ and α - $3d_{x^2-y^2}$ MOs and degenerate β - $3d_{xy}$ and β - $3d_{x^2-y^2}$ ($\text{Mn}^{\text{V}}-\text{N}_{\text{eq}}$ σ^*) MOs. These sets of α - and β -spin orbitals are split by only 0.4 eV, reflecting the smaller spin polarization in the $S = 1$ complex, and contain a total of 7.7% Mn 4p character. This enhanced Mn 3d-4p_{xy} mixing is due to the shorter $\text{Mn}^{\text{V}}-\text{N}_{\text{eq}}$ distances in the oxomanganese(V) complex (Figure 11, right). The higher-energy band at 6542.8 eV for $[\text{Mn}^{\text{V}}(\text{O})(\text{H}_3\text{buea})]$ arises from two excitations terminating in the α - and β - $3d_z^2$ orbitals that are split by ~0.6 eV and contain 3.4% Mn 4p character. Compared to $[\text{Mn}^{\text{IV}}(\text{O})(\text{H}_3\text{buea})]^-$, the transition into the β - $3d_z^2$ orbital is blue-shifted by 0.7 eV for $[\text{Mn}^{\text{V}}(\text{O})(\text{H}_3\text{buea})]$, consistent with the higher Mn oxidation state.

The calculated pre-edge properties of $[\text{Mn}^{\text{V}}(\text{O})(\text{H}_3\text{buea})]$ are in excellent agreement with the correlations observed for the oxo- and hydroxomanganese(IV) complexes (Figure 8). The overall calculated pre-edge area of $[\text{Mn}^{\text{V}}(\text{O})(\text{H}_3\text{buea})]$ is only ~20% greater than that of $[\text{Mn}^{\text{IV}}(\text{O})(\text{H}_3\text{buea})]^-$ (17.5 and 20.9, respectively) and falls within the range of calculated areas for the $\text{Mn}^{\text{IV}}=\text{O}$ species (15.1–27.8). Low-spin oxomanganese(V) complexes with much shorter Mn–O bond lengths (~1.54 Å) show much more intense pre-edge transitions.^{23,24,35} Thus, if a trigonal bipyramidal $\text{Mn}^{\text{V}}=\text{O}$ adduct were to be formed during OEC turnover, it would present a very modest pre-edge feature that could easily be mistaken for that of an $\text{Mn}^{\text{IV}}=\text{O}$ species.

CONCLUSIONS

We have applied a combined experimental and computational analysis to understand the pre-edge properties of oxo- and hydroxomanganese(IV) complexes and an $S = 1$ oxomanganese(V) species. Using detailed assignments of pre-edge features developed using TD-DFT computations, the intense pre-edge features of $\text{Mn}^{\text{IV}}=\text{O}$ adducts are primarily attributed to excitations to the $\text{Mn}=\text{O}$ σ^* MOs that contain significant 3d-4p mixing. Nonetheless, the intensities and breadths of the pre-edge signals are strongly influenced not only by the $\text{Mn}=\text{O}$ distance but also the local coordination geometry of the Mn center. For example, significant Mn 3d-

4p_{xy} mixing in trigonal bipyramidal Mn-oxo adducts increases the breadth of the pre-edge signal. In particular, our computations provide strong evidence that $\text{Mn}^{\text{IV}}-\text{OH}$, $\text{Mn}^{\text{IV}}=\text{O}$, and even $\text{Mn}^{\text{V}}=\text{O}$ species can show pre-edge peaks of comparable area and height, dependent on the specifics of the ligand field. Thus, great caution should be taken in making structural assignments regarding such complexes on the basis of pre-edge data alone.

ASSOCIATED CONTENT

Supporting Information

Complete EXAFS fittings results, fits to XANES spectra of 2 and 3, detailed information regarding calculated pre-edge properties, Mn 3d orbital splitting diagram of $[\text{Mn}^{\text{V}}(\text{O})(\text{H}_3\text{buea})]$, and Cartesian coordinates for all DFT-optimized models. This material is available free of charge via the Internet at <http://pubs.acs.org>.

AUTHOR INFORMATION

Corresponding Author

*Address: 1251 Wescoe Hall Drive Lawrence, KS 66045. Phone: (785) 864-3968. Fax: (785) 864-5396. E-mail: taj@ku.edu.

Notes

The authors declare no competing financial interest.

ACKNOWLEDGMENTS

This work was supported by the US NSF (CHE-1056470 to T.A.J.). XAS experiments were supported by the Center for Synchrotron Biosciences grant, P30-EB-009998, from the National Institute of Biomedical Imaging and Bioengineering (NIBIB). We thank Prof. Daryle Busch for providing a gift of the $[\text{Mn}^{\text{II}}(\text{Cl}_2)(\text{Me}_2\text{EBC})]$ complex and Dr. Erik Farquhar at NSLS for outstanding support of our XAS experiments and helpful discussions.

REFERENCES

- (1) Wu, A. J.; Penner-Hahn, J. E.; Pecoraro, V. L. *Chem. Rev.* **2004**, *104*, 903–938.
- (2) Yachandra, V. K. *Adv. Photosynth. Respir.* **2005**, *22*, 235–260.
- (3) Penner-Hahn, J. Structural characterization of the Mn site in the photosynthetic oxygen-evolving complex. In *Metal Sites in Proteins and Models Redox Centres*, Hill, H. A. O., Sadler, P. J., Thomson, A. J., Eds.; Springer: Berlin, 1998; Vol. 90, pp 1–36.
- (4) Yachandra, V. K.; Sauer, K.; Klein, M. P. *Chem. Rev.* **1996**, *96*, 2927–2950.
- (5) Yano, J.; Yachandra, V. *Photosynth. Res.* **2009**, *102*, 241–254.
- (6) McEvoy, J. P.; Brudvig, G. W. *Chem. Rev.* **2006**, *106*, 4455–4483.
- (7) Pecoraro, V. L.; Hsieh, W.-Y. *Inorg. Chem.* **2008**, *47*, 1765–1778.
- (8) Robblee, J. H.; Messinger, J.; Cinco, R. M.; McFarlane, K. L.; Fernandez, C.; Pizarro, S. A.; Sauer, K.; Yachandra, V. K. *J. Am. Chem. Soc.* **2002**, *124*, 7459–7471.
- (9) Waldo, G. S.; Penner-Hahn, J. E. *Biochemistry* **1995**, *34*, 1507–1512.
- (10) Ayougou, K.; Bill, E.; Charnock, J. M.; Garner, C. D.; Mandon, D.; Trautwein, A. X.; Weiss, R.; Winkler, H. *Angew. Chem., Int. Ed. Engl.* **1995**, *34*, 343–346.
- (11) Bortolini, O. *Nouv. J. Chim.* **1986**, *10*, 39–49.
- (12) Chen, J.; Lee, Y.-M.; Davis, K. M.; Wu, X.; Seo, M. S.; Cho, K.-B.; Yoon, H.; Park, Y. J.; Fukuzumi, S.; Pushkar, Y. N.; Nam, W. *J. Am. Chem. Soc.* **2013**, *135*, 6388–6391.
- (13) Kurahashi, T.; Kikuchi, A.; Shiro, Y.; Hada, M.; Fujii, H. *Inorg. Chem.* **2010**, *49*, 6664–6672.
- (14) Kurahashi, T.; Kikuchi, A.; Tosha, T.; Shiro, Y.; Kitagawa, T.; Fujii, H. *Inorg. Chem.* **2008**, *47*, 1674–1686.

- (15) Leto, D. F.; Ingram, R.; Day, V. W.; Jackson, T. A. *Chem. Commun.* **2013**, 49, 5378–5380.
- (16) Wu, X.; Seo, M. S.; Davis, K. M.; Lee, Y.-M.; Chen, J.; Cho, K.-B.; Pushkar, Y. N.; Nam, W. *J. Am. Chem. Soc.* **2011**, 133, 20088–20091.
- (17) Arunkumar, C.; Lee, Y.-M.; Lee, J. Y.; Fukuzumi, S.; Nam, W. *Chem.—Eur. J.* **2009**, 15, 11482–11489.
- (18) Chattopadhyay, S.; Geiger, R. A.; Yin, G.; Busch, D. H.; Jackson, T. A. *Inorg. Chem.* **2010**, 49, 7530–7535.
- (19) Garcia-Bosch, I.; Company, A.; Cady, C. W.; Styring, S.; Browne, W. R.; Ribas, X.; Costas, M. *Angew. Chem., Int. Ed. Engl.* **2011**, 50, 5648–5653.
- (20) Parsell, T. H.; Behan, R. K.; Green, M. T.; Hendrich, M. P.; Borovik, A. S. *J. Am. Chem. Soc.* **2006**, 128, 8728–8729.
- (21) Sawant, S. C.; Wu, X.; Cho, J.; Cho, K.-B.; Kim, S. H.; Seo, M. S.; Lee, Y.-M.; Kubo, M.; Ogura, T.; Shaik, S.; Nam, W. *Angew. Chem., Int. Ed. Engl.* **2010**, 49, 8190–8194.
- (22) Yin, G.; Danby, A. M.; Kitko, D.; Carter, J. D.; Scheper, W. M.; Busch, D. H. *J. Am. Chem. Soc.* **2007**, 129, 1512–1513.
- (23) Collins, T. J.; Gordon-Wylie, S. W. *J. Am. Chem. Soc.* **1989**, 111, 4511–4513.
- (24) Collins, T. J.; Powell, R. D.; Slebodnick, C.; Uffelman, E. S. *J. Am. Chem. Soc.* **1990**, 112, 899–901.
- (25) MacDonnell, F. M.; Fackler, N. L. P.; Stern, C.; O'Halloran, T. V. *J. Am. Chem. Soc.* **1994**, 116, 7431–7432.
- (26) Miller, C. G.; Gordon-Wylie, S. W.; Horwitz, C. P.; Strazisar, S. A.; Peraino, D. K.; Clark, G. R.; Weintraub, S. T.; Collins, T. J. *J. Am. Chem. Soc.* **1998**, 120, 11540–11541.
- (27) Yin, G.; McCormick, J. M.; Buchalova, M.; Danby, A. M.; Rodgers, K.; Day, V. W.; Smith, K.; Perkins, C. M.; Kitko, D.; Carter, J. D.; Scheper, W. M.; Busch, D. H. *Inorg. Chem.* **2006**, 45, 8052–8061.
- (28) Yano, J.; Kern, J.; Irrgang, K.-D.; Latimer, M. J.; Bergmann, U.; Glatzel, P.; Pushkar, Y.; Biesiadka, J.; Loll, B.; Sauer, K.; Messinger, J.; Zouni, A.; Yachandra, V. K. *Proc. Natl. Acad. Sci. U. S. A.* **2005**, 102, 12047–12052.
- (29) Chandrasekaran, P.; Stieber, S. C. E.; Collins, T. J.; Que, L., Jr.; Neese, F.; DeBeer, S. *Dalton Trans.* **2011**, 40, 11070–11079.
- (30) DeBeer George, S.; Petrenko, T.; Neese, F. *J. Phys. Chem. A* **2008**, 112, 12936–12943.
- (31) Westre, T. E.; Kennepohl, P.; DeWitt, J. G.; Hedman, B.; Hodgson, K. O.; Solomon, E. I. *J. Am. Chem. Soc.* **1997**, 119, 6297–6314.
- (32) Randall, C. R.; Shu, L.; Chiou, Y.-M.; Hagen, K. S.; Ito, M.; Kitajima, N.; Lachicotte, R. J.; Zang, Y.; Que, L., Jr. *Inorg. Chem.* **1995**, 34, 1036–1039.
- (33) DeBeer George, S.; Brant, P.; Solomon, E. I. *J. Am. Chem. Soc.* **2005**, 127, 667–674.
- (34) Roemelt, M.; Beckwith, M. A.; Duboc, C.; Collomb, M.-N.; Neese, F.; DeBeer, S. *Inorg. Chem.* **2011**, 51, 680–687.
- (35) Lansky, D. E.; Mandimutsira, B.; Ramdhanie, B.; Clausen, M.; Penner-Hahn, J.; Zvyagin, S. A.; Telsler, J.; Zhan, R.; Ou, Z.; Kadish, K. M.; Zakharov, L.; Rheingold, A. L.; Goldberg, D. P. *Inorg. Chem.* **2005**, 44, 4485–4498.
- (36) Weng, T.-C.; Hsieh, W.-Y.; Uffelman, E. S.; Gordon-Wylie, S. W.; Collins, T. J.; Pecoraro, V. L.; Penner-Hahn, J. E. *J. Am. Chem. Soc.* **2004**, 126, 8070–8071.
- (37) Yano, J.; Robblee, J.; Pushkar, Y.; Marcus, M. A.; Bendix, J.; Workman, J. M.; Collins, T. J.; Solomon, E. I.; DeBeer George, S.; Yachandra, V. K. *J. Am. Chem. Soc.* **2007**, 129, 12989–13000.
- (38) Song, W. J.; Seo, M. S.; DeBeer George, S.; Ohta, T.; Song, R.; Kang, M. J.; Toshi, T.; Kitagawa, T.; Solomon, E. I.; Nam, W. *J. Am. Chem. Soc.* **2007**, 129, 1268–1277.
- (39) England, J.; Martinho, M.; Farquhar, E. R.; Frisch, J. R.; Bominaar, E. L.; Münck, E.; Que, L., Jr. *Angew. Chem., Int. Ed. Engl.* **2009**, 48, 3622–3626.
- (40) Jackson, T. A.; Rohde, J.-U.; Seo, M. S.; Sastri, C. V.; DeHont, R.; Ohta, T.; Stubna, A.; Kitagawa, T.; Münck, E.; Nam, W.; Que, L., Jr. *J. Am. Chem. Soc.* **2008**, 130, 12394–12407.
- (41) Rohde, J.-U.; Torelli, S.; Shan, X.; Lim, M. H.; Klinker, E. J.; Kaizer, J.; Chen, K.; Nam, W.; Que, L., Jr. *J. Am. Chem. Soc.* **2004**, 126, 16750–16761.
- (42) Lassalle-Kaiser, B.; Hureau, C.; Pantazis, D. A.; Pushkar, Y.; Guillot, R.; Yachandra, V. K.; Yano, J.; Neese, F.; Anxolabéhère-Mallart, E. *Energy Environ. Sci.* **2010**, 3, 924–938.
- (43) Banerjee, P.; Sproules, S.; Weyhermüller, T.; DeBeer George, S.; Wieghardt, K. *Inorg. Chem.* **2009**, 48, 5829–5847.
- (44) Krewald, V.; Lassalle-Kaiser, B.; Boron, T. T.; Pollock, C. J.; Kern, J.; Beckwith, M. A.; Yachandra, V. K.; Pecoraro, V. L.; Yano, J.; Neese, F.; DeBeer, S. *Inorg. Chem.* **2013**, 52, 12904–12914.
- (45) Yin, G.; Danby, A. M.; Kitko, D.; Carter, J. D.; Scheper, W. M.; Busch, D. H. *J. Am. Chem. Soc.* **2008**, 130, 16245–16253.
- (46) George, G. N. EXAFSPAK; Stanford Synchrotron Radiation Laboratory; Stanford, CA, 1990.
- (47) Rehr, J. J.; Mustre de Leon, J.; Zabinsky, S. I.; Albers, R. C. *J. Am. Chem. Soc.* **1991**, 113, 5135–5140.
- (48) Neese, F., ORCA - an ab initio, Density Functional and Semiempirical Program Package, Version 2.9, University of Bonn: Bonn, 2012.
- (49) Becke, A. D. *Phys. Rev. A: At, Mol., Opt. Phys.* **1988**, 38, 3098.
- (50) Perdew, J. P. *Phys. Rev. B* **1986**, 33, 8822–8824.
- (51) Schäfer, A.; Horn, H.; Ahlrichs, R. *J. Chem. Phys.* **1992**, 97, 2571–2577.
- (52) Schäfer, A.; Huber, C.; Ahlrichs, R. *J. Chem. Phys.* **1994**, 100, 5829–5835.
- (53) Neese, F. *J. Comput. Chem.* **2003**, 24, 1740–1747.
- (54) Hubin, T. J.; McCormick, J. M.; Collinson, S. R.; Buchalova, M.; Perkins, C. M.; Alcock, N. W.; Kahol, P. K.; Raghunathan, A.; Busch, D. H. *J. Am. Chem. Soc.* **2000**, 122, 2512–2522.
- (55) Dey, A.; Hocking, R. K.; Larsen, P.; Borovik, A. S.; Hodgson, K. O.; Hedman, B.; Solomon, E. I. *J. Am. Chem. Soc.* **2006**, 128, 9825–9833.
- (56) Hirata, S.; Head-Gordon, M. *Chem. Phys. Lett.* **1999**, 302, 375–382.
- (57) Hirata, S.; Head-Gordon, M. *Chem. Phys. Lett.* **1999**, 314, 291–299.
- (58) Becke, A. D. *J. Chem. Phys.* **1993**, 98, 1372–1377.
- (59) Becke, A. D. *J. Chem. Phys.* **1993**, 98, 5648–5652.
- (60) Lee, C.; Yang, W.; Parr, R. G. *Phys. Rev. B* **1988**, 37, 785–789.
- (61) Weigend, F.; Ahlrichs, R. *Phys. Chem. Chem. Phys.* **2005**, 7, 3297–3305.
- (62) Lenthe, E. v.; Baerends, E. J.; Snijders, J. G. *J. Chem. Phys.* **1993**, 99, 4597–4610.
- (63) van Wüllen, C. *J. Chem. Phys.* **1998**, 109, 392–399.
- (64) Klamt, A.; Schuurmann, G. *J. Chem. Soc., Perkin Trans. 2* **1993**, 799–805.
- (65) XAS data were collected for several samples of **2** and **3**, with each sample prepared from different batches of $2(\text{PF}_6)_2$, over multiple trips to the beamline. None of the samples of **2** showed evidence of photoreduction while all of the samples of **3** were photosensitive. Thus, the photoreduction of **3** is not caused by a contaminant appearing in a single sample.
- (66) Dubois, L.; Jacquamet, L.; Pecaut, J.; Latour, J.-M. *Chem. Commun.* **2006**, 4521–4523.
- (67) Shadle, S. E.; Penner-Hahn, J. E.; Schugar, H. J.; Hedman, B.; Hodgson, K. O.; Solomon, E. I. *J. Am. Chem. Soc.* **1993**, 115, 767–776.
- (68) Kelly, S. D.; Bare, S. R.; Greenlay, N.; Azevedo, G.; Balasubramanian, M.; Barton, D.; Chattopadhyay, S.; Fakra, S.; Johannessen, B.; Newville, M.; Pena, J.; Pokrovski, G. S.; Proux, O.; Priolkar, K.; Ravel, B.; Webb, S. M. *J. Phys.: Conference Ser.* **2009**, 190, 012032.
- (69) Gray, H. B. *Electrons and Chemical Bonding*; W. A. Benjamin: New York, 1964; p xv, 223.
- (70) Green, M. T. *J. Am. Chem. Soc.* **2006**, 128, 1902–1906.
- (71) Neese, F. *J. Biol. Inorg. Chem.* **2006**, 11, 702–711.
- (72) Berry, J. F.; DeBeer George, S.; Neese, F. *Phys. Chem. Chem. Phys.* **2008**, 10, 4361–4374.
- (73) Farges, F. *Phys. Rev. B* **2005**, 71, 155109.

(74) Glatzel, P.; Bergmann, U.; Yano, J.; Visser, H.; Robblee, J. H.; Gu, W.; de Groot, F. M. F.; Christou, G.; Pecoraro, V. L.; Cramer, S. P.; Yachandra, V. K. *J. Am. Chem. Soc.* **2004**, *126*, 9946–9959.

(75) Haumann, M.; Liebisch, P.; Müller, C.; Barra, M.; Grabolle, M.; Dau, H. *Science* **2005**, *310*, 1019–1021.

(76) Taguchi, T.; Gupta, R.; Lassalle-Kaiser, B.; Boyce, D. W.; Yachandra, V. K.; Tolman, W. B.; Yano, J.; Hendrich, M. P.; Borovik, A. S. *J. Am. Chem. Soc.* **2012**, *134*, 1996–1999.